bioRxiv preprint doi: https://doi.org/10.1101/857961; this version posted November 29, 2019. The copyright holder for this preprint (which was not certified by peer review) is the author/funder, who has granted bioRxiv a license to display the preprint in perpetuity. It is made available under aCC-BY-NC 4.0 International license.

Selective metabolic redundancy of Gpi1 allows for specific inhibition of inflammatory Th17 cells

Lin Wu[1,3,7], Kate E.R. Hollinshead[2], Yuhan Hao[3,4], Christy Au[1,5], Lina Kroehling[1], Charles Ng[1], Woan-Yu Lin[1], Dayi Li[1], Hernandez Moura Silva[1], Jong Shin[6], Juan J. Lafaille[1,6], Richard Possemato[6], Michael E. Pacold[2], Thales Y. Papagiannakopoulos[6], Alec C. Kimmelman[2], Rahul Satija[3,4], Dan R. Littman[1,5,6,7]

[1]The Kimmel Center for Biology and Medicine of the Skirball Institute, New York University School of Medicine, New York, NY, USA; [2]Department of Radiation Oncology and Perlmutter Cancer Center, New York University School of Medicine, New York, NY, USA; [3]New York Genome Center, New York, NY, USA; [4]Center for Genomics and Systems Biology, New York University, New York, NY, USA; [5]Howard Hughes Medical Institute, New York, NY, USA; [6]Department of Pathology, New York University School of Medicine, New York, NY, USA.

Correspondence: lin.wu@med.nyu.edu and dan.littman@med.nyu.edu

Key words: Hypoxia, autoimmunity, CRISPR, OXPHOS, inflammation, segmented filamentous bacteria, EAE, colitis

bioRxiv preprint doi: https://doi.org/10.1101/857961; this version posted November 29, 2019. The copyright holder for this preprint (which was not certified by peer review) is the author/funder, who has granted bioRxiv a license to display the preprint in perpetuity. It is made available under aCC-BY-NC 4.0 International license.

Abstract

Targeting glycolysis has been considered therapeutically intractable owing to its essential housekeeping role. However, the context-dependent requirement for individual glycolytic steps has not been fully explored. We show that CRISPR-mediated targeting of glycolysis in T cells in mice results in global loss of Th17 cells, whereas deficiency of the glycolytic enzyme glucose phosphate isomerase (Gpi1) selectively eliminates inflammatory encephalitogenic and colitogenic Th17 cells, without substantially affecting homeostatic microbiota-specific Th17 cells. In homeostatic Th17 cells, partial blockade of glycolysis upon *Gpi1* inactivation was compensated by pentose phosphate pathway flux and increased mitochondrial respiration. In contrast, inflammatory Th17 cells experience a hypoxic microenvironment known to limit mitochondrial respiration, which is incompatible with loss of *Gpi1*. Our study suggests that inhibiting glycolysis by targeting Gpi1 could be an effective therapeutic strategy with minimum toxicity for Th17-mediated autoimmune diseases, and, more generally, that metabolic redundancies can be exploited for selective targeting of disease processes.

bioRxiv preprint doi: https://doi.org/10.1101/857961; this version posted November 29, 2019. The copyright holder for this preprint (which was not certified by peer review) is the author/funder, who has granted bioRxiv a license to display the preprint in perpetuity. It is made available under aCC-BY-NC 4.0 International license.

Introduction

Cellular metabolism is a dynamic process that supports all aspects of the cell's activities. It is orchestrated by more than 2000 metabolic enzymes organized into pathways that are specialized for processing and producing distinct metabolites. Multiple metabolites are shared by different pathways, serving as nodes in a complex network with many redundant elements. A well-appreciated example of metabolic plasticity is the generation of ATP by either glycolysis or by mitochondrial oxidative phosphorylation (OXPHOS), making the two processes partially redundant despite having many other non-redundant functions. Here, we explore metabolic plasticity in the context of T cell function and microenvironment, and the consequence of limiting that plasticity by inhibiting specific metabolic enzymes.

Th17 cells are a subset of $CD4^+$ T cells whose differentiation is governed by the transcription factor RORγt, which regulates the expression of the signature cytokines IL-17A and IL-17F (Ivanov et al., 2006). Under homeostatic conditions, Th17 cells typically reside at mucosal surfaces where they provide protection from pathogenic bacteria and fungi and also regulate the composition of the microbiota (Kumar et al., 2016; Mao et al., 2018; Milner and Holland, 2013; O'Quinn et al., 2008; Okada et al., 2015; Puel et al., 2011). However, under conditions that favor inflammatory processes, due to environmental and/or genetic factors, Th17 cells can adopt a pro-inflammatory program that promotes autoimmune diseases, including inflammatory bowel disease (Hue et al., 2006; Kullberg et al., 2006), psoriasis (Piskin et al., 2006; Zheng et al., 2007), and diverse forms of arthritis (Hirota et al., 2007; Murphy et al., 2003; Nakae et al., 2003a; Nakae et al., 2003b). This program is dependent on IL-23 and is typically marked by the additional expression in T cells of T-bet and IFN-γ, with or without expression of IL-17A or IL-17F (Ahern et al., 2010; Cua et al., 2003; Hirota et al., 2011; Morrison et al., 2013). The Th17

bioRxiv preprint doi: https://doi.org/10.1101/857961; this version posted November 29, 2019. The copyright holder for this preprint (which was not certified by peer review) is the author/funder, who has granted bioRxiv a license to display the preprint in perpetuity. It is made available under aCC-BY-NC 4.0 International license.

63 pathway has been targeted with neutralizing antibodies specific for IL-17A and IL-23 to
64 effectively treat psoriasis and some forms of arthritis, but these therapies inevitably expose
65 patients to potential fungal and bacterial infections, as they also inhibit homeostatic Th17 cell
66 functions. In this study, we aimed to identify genes and pathways that are required for the
67 function of inflammatory pathogenic Th17 cells, but are dispensable for homeostatic Th17 cells,
68 which may enable the selective therapeutic targeting of pathogenic Th17 cells.
69 T cell activation leads to extensive clonal expansion, demanding a large amount of energy
70 and biomass production. Such demand is fulfilled by enhanced metabolic activities, including
71 activation of pro-growth signals, particularly Mammalian Target Of Rapamycin (mTOR)
72 (Delgoffe et al., 2009; Powell et al., 2012), and activation of glycolysis, the pentose phosphate
73 pathway (PPP), glutaminolysis, and lipid synthesis for anabolic reactions (Berod et al., 2014;
74 Fox et al., 2005; Gerriets and Rathmell, 2012; Johnson et al., 2018; Palmer et al., 2015; Patel and
75 Powell, 2017; Shi et al., 2011). Glycolysis is central both in generating ATP and providing
76 building blocks for macromolecular biosynthesis. Glycolysis catabolizes glucose into pyruvate
77 through ten enzymatic reactions. In normoxic environments, pyruvate is typically transported
78 into the mitochondria to be processed by OXPHOS for ATP production. In hypoxic
79 environments, OXPHOS is suppressed and glycolysis is enhanced, generating lactate from
80 pyruvate in order to regenerate nicotinamide adenine dinucleotide (NAD^+) needed to support
81 ongoing glycolytic flux (Birsoy et al., 2015; Semenza, 2014; Sullivan et al., 2015). In highly
82 proliferating cells, such as cancer cells and activated T cells, pyruvate can be converted into
83 lactate in the presence of oxygen, a phenomenon termed aerobic glycolysis, or the "Warburg
84 effect" (MacIver et al., 2013; Vander Heiden et al., 2009; Warburg et al., 1958). Although
85 inhibiting glycolysis is an effective method of blocking T cell activation *in vitro* (Shi et al.,

bioRxiv preprint doi: https://doi.org/10.1101/857961; this version posted November 29, 2019. The copyright holder for this preprint (which was not certified by peer review) is the author/funder, who has granted bioRxiv a license to display the preprint in perpetuity. It is made available under aCC-BY-NC 4.0 International license.

2011), inhibition *in vivo*, for example with 2-Deoxy-D-glucose (2DG), has limited application in patients, due to toxic side effects as a result of the housekeeping function of glycolysis in multiple cell types (Raez et al., 2013).

Here, we systematically interrogate the requirement for individual glycolytic reactions in Th17 cell models of inflammation and homeostatic function. We found that the glycolysis gene *Gpi1* is unique in that it is selectively required by inflammatory pathogenic Th17 but not homeostatic Th17 cells. All other tested glycolysis genes were essential for functions of both Th17 cell types. Our mechanistic study revealed that upon Gpi1 loss during homeostasis, Pentose Phosphate Pathway (PPP) activity was sufficient to maintain basal glycolytic flux for biomass generation, while increased mitochondrial respiration compensated for reduced glycolytic flux. In contrast, Th17 cells in the inflammation models are confined to hypoxic environments and hence were unable to increase respiration to compensate for reduced glycolytic flux. This metabolic stress led to the selective elimination of Gpi1-deficient Th17 cells in inflammatory settings but not in healthy intestinal lamina propria. Overall, our study reveals a context-dependent metabolic requirement that can be targeted to eliminate pathogenic Th17 cells. As Gpi1 blockade can be better tolerated than inhibition of other glycolysis components, it is a potentially attractive target for clinical use.

Results

Inflammatory Th17 cells have higher expression of glycolysis pathway genes than commensal bacteria-induced homeostatic Th17 cells

bioRxiv preprint doi: https://doi.org/10.1101/857961; this version posted November 29, 2019. The copyright holder for this preprint (which was not certified by peer review) is the author/funder, who has granted bioRxiv a license to display the preprint in perpetuity. It is made available under aCC-BY-NC 4.0 International license.

Commensal SFB induce the generation of homeostatic Th17 cells in the small intestine lamina propria (SILP) (Ivanov et al., 2009), whereas immunization with myelin oligodendrocyte glycoprotein peptide (MOG) in complete Freund's adjuvant (CFA) induces pathogenic Th17 cells in the spinal cord (SC), resulting in experimental autoimmune encephalomyelitis (EAE) (Cua et al., 2003). Th17 cell pathogenicity requires expression of IL-23R (Ahern et al., 2010; McGeachy et al., 2009). To identify genes involved in the pathogenic but not the homeostatic Th17 cell program, we reconstituted Rag1$^{-/-}$ mice with isotype-marked *Il23r*-sufficient (*Il23r*$^{GFP/+}$) and *Il23r* knockout (*Il23r*$^{GFP/GFP}$) bone marrow cells, and sorted CD4^{+} T cells of both genetic backgrounds from the SILP of SFB-colonized mice and the SC of EAE mice for single cell RNA sequencing (scRNAseq) analysis (Figure S1A, described in detail in Methods). We identified 4 clusters of CD4^{+} T cells in the SC of EAE mice and 5 clusters of CD4^{+} T cells in ileum lamina propria of SFB-colonized mice (Figure S1B,C)). Clusters were annotated based on their signature genes, i.e. Th17 cells (*Il17a*), Th1 cells (*Ifng*), Treg cells (*Foxp3*), and Tcf7^{+} cells (*Tcf7*) (Figure S1D,E). Importantly, two of the EAE clusters consist mostly of Il-23R-sufficient T cells (Figure S1G,H), indicating that these populations are likely pathogenic. One of them was annotated as Th17 and the other as Th1* according to earlier publications describing such cells as *Il23r*-dependent IFN-γ producers (Okada et al., 2015), and they were validated using flow cytometry (Figure S1I). Importantly, pathway enrichment analysis revealed glycolysis as the top pathway upregulated in both EAE Th17 and Th1* compared to the SFB-induced Th17 cells (Figures S1J,K).

We selected a subset of genes that were differentially expressed in the pathogenic Th17/Th1* cells (EAE model) versus the homeostatic Th17 cells (SFB model) for pilot functional studies (Figures S1L,M). We developed a CRISPR- based T cell transfer EAE system to evaluate the

bioRxiv preprint doi: https://doi.org/10.1101/857961; this version posted November 29, 2019. The copyright holder for this preprint (which was not certified by peer review) is the author/funder, who has granted bioRxiv a license to display the preprint in perpetuity. It is made available under aCC-BY-NC 4.0 International license.

roles of the selected genes in pathogenicity (Figures S2A-C; see Methods). Among 12 genes tested, only triosephosphate isomerase 1 (*Tpi1*), encoding an enzyme in the glycolysis pathway, was required for disease onset following transfer of in vitro differentiated MOG-specific 2D2 TCR transgenic T cells (Figure S2D). This result was confirmed by analyzing *Tpi1*$^{f/f}$*Cd4*^{cre} mice, which, unlike Tpi1$^{+/+}$ CD4^{cre} littermates, were completely resistant to EAE induction (Figure 1A). This finding prompted us to direct our focus on the glycolysis pathway. The relatively sparse scRNAseq data detected the transcripts of only a few glycolysis pathway genes. We therefore compared bulk RNAseq data of the two major pathogenic populations (Th1*: Klrc1^{+} Foxp3^{RFP-}, Th17: IL17a^{GFP+} Klrc1^{-} Foxp3^{RFP-}) and the Treg cells (Foxp3^{RFP+} IL17a^{GFP-}) from the spinal cord of EAE model mice to data from the Th17 (IL17a^{GFP+} Foxp3^{RFP-}) and Treg (IL17a^{GFP-} Foxp3^{RFP+}) cells from the SILP of the SFB model (Figures S2E, F). We found that almost every glycolysis pathway gene was expressed at a higher level in the EAE model than in the SILP CD4^{+} T cells, irrespective of whether cells were pathogenic or Treg (Figure 1B), suggesting that most CD4^{+} T cells have more active glycoysis in the inflamed spinal cord microenvironment than in the SILP at homeostasis.

Despite these differences in gene expression, Tpi1 was also indispensable for the SFB-dependent induction of homeostatic Th17 cells. We analyzed CD4^{+} T cell profiles in chimeric *Rag1* KO mice reconstituted with a 1:1 mix of bone marrow cells from *Tpi1*$^{+/+}$*CD4*^{cre} CD45.1/2 and *Tpi1*$^{f/f}$*CD4*^{cre} CD45.2/2 donors (Figure S3A). Tpi1 deficiency led to 33-fold reduction of total CD4^{+} T cells in the SILP and to 1.4-fold and 1.7-fold reduction in the mLN and the peripheral blood, respectively (Figure 1D). Moreover, RORγt, Foxp3, IL-17a, and IFN-γ were all severely reduced in mutant T cells relative to the WT cells in the SILP and mLN (Figures S3A,B). The same pattern was observed in the EAE model, using mixed bone marrow chimeric

bioRxiv preprint doi: https://doi.org/10.1101/857961; this version posted November 29, 2019. The copyright holder for this preprint (which was not certified by peer review) is the author/funder, who has granted bioRxiv a license to display the preprint in perpetuity. It is made available under aCC-BY-NC 4.0 International license.

mice (Figures 1E, and S3C), indicating that Tpi1 is required for the differentiation of all $CD4^+$ T cell subsets.

Gpi1 is selectively required by inflammatory but not homeostatic Th17 cells

The higher glycolytic activity of the inflammatory Th17 cells suggested that they may be more sensitive than the homeostatic Th17 cells to inhibition of glycolysis. However, neither cell type is likely to survive a complete block in glycolysis (as achieved by Gapdh knockout). Inhibition of several glycolysis genes (Tpi1, Gpi1, Ldha, explained in figure S4A) may result in attenuation rather than complete blockade of the pathway. We therefore tested whether deficiency of additional glycolysis pathway genes would selectively impair Th17 cells in inflammatory conditions. To do so, we assessed the ability of co-tranferred control and targeted TCR transgenic T cells to differentiate into Th17 cells in models of homeostasis (7B8 T cells in SFB-colonized mice (Yang et al., 2014)) and inflammatory disease (2D2 T cells for EAE (Bettelli et al., 2003) and HH7.2 T cells for *Helicobacter*-dependent transfer colitis (Xu et al., 2018)) (Figure 2A). The genes of interest (indicated in Figure S4A) or the control gene *Olfr2* were inactivated by guide RNA electroporation of naïve isotype-marked $CD4^+$ TCR and Cas9 transgenic T cells (Platt et al., 2014), which were then transferred in equal numbers into recipient mice (Figures 2A, S4B). Targeting was performed with sgRNAs that achieved the highest in vitro knockout efficiency (~80-90%) (Figures S4C-E), which corresponded to the frequency of targeted cells at 4 days after electroporation and transfer into mice, as assessed by targeting of GFP (Figure S4B). This strategy also allowed for efficient double gene KO (Figure S4F).

We first evaluated this T cell transfer system with Tpi1 guide RNA electroporation, and compared to the results with mixed bone marrow chimeras generated with control and *Tpi1*-

bioRxiv preprint doi: https://doi.org/10.1101/857961; this version posted November 29, 2019. The copyright holder for this preprint (which was not certified by peer review) is the author/funder, who has granted bioRxiv a license to display the preprint in perpetuity. It is made available under aCC-BY-NC 4.0 International license.

177 deficient progenitors. In both SFB and EAE T cell transfer experiments, there were roughly 9-
178 fold fewer *Tpi1*-targeted than co-transferred control Th17 cells in the SILP or the SC,
179 respectively (Figures 2B-D). The reduction in cell number was consistent with the *in vitro* KO
180 efficiency as shown by the immunoblot data (Figure S4C), suggesting that the majority of the
181 *Tpi1* KO cells were eliminated in the total T cell pool, and that the remaining cells were likely
182 not targeted. This is supported by the finding of similar proportions of cells expressing RORγt
183 and IL-17a in control and Tpi1-targeted populations (Figures S5A-D), which was not observed in
184 the bone marrow-reconstituted mice (Figures S3B). Collectively, these results indicated that the
185 electroporation transfer system could be successfully used to evaluate T cell gene functions *in*
186 *vivo*.

187 Similar to the *Tpi1* KO, cells deficient for *Gapdh* were eliminated in all three models tested
188 (Figures 2B-E). Inactivation of *Ldha* resulted in loss of the cells in the EAE model, and a less
189 striking, but still substantial, cell number reduction in the homeostatic SFB model (Figures 2B-
190 E). In contrast, although *Gpi1* ablation reduced cell number by 75% in the inflammatory EAE
191 and colitis models, it had no significant effect on cell number in the homeostatic Th17 cell model
192 (Figures 2B-E). Consistent with the reduction in cell number, *Gpi1*-mutant 2D2 cells were
193 unable to induce EAE (Figure 2F), suggesting that Gpi1 is essential for pathogenicity. We also
194 investigated Th17 cell differentiation and cytokine production by *Gpi1*-deficient cells in the SFB
195 model, and found no difference from co-transferred control cells in terms of RORγt/Foxp3
196 expression (Figures 2G) or IL-17a production, as demonstrated using 7B8 cells from mice bred
197 to the *Il17a*$^{GFP/+}$ reporter strain (Fig. 2H). This suggests that SFB-specific T cell differentiation
198 and cytokine production are not affected by Gpi1 deficiency.

bioRxiv preprint doi: https://doi.org/10.1101/857961; this version posted November 29, 2019. The copyright holder for this preprint (which was not certified by peer review) is the author/funder, who has granted bioRxiv a license to display the preprint in perpetuity. It is made available under aCC-BY-NC 4.0 International license.

Because of the very small number of 7B8 cells that could be isolated from the SILP in the mixed chimera experiments, we were unable to confirm loss of Gpi1 by immunoblotting, but there was consistent reduction of IL-17a in *Gpi1*-targeted 7B8 cells isolated from the SILP and re-stimulated in vitro. A similar phenotype was observed for *Ldha* KO 7B8 cells (Figures S5C,D), but not in *Olfr2* targeted cells. While the reduced cytokine production observed in the *in vitro* restimulation assay supports the maintainence of Gpi1-deficient cells in the SILP, it is not necessarily contradictory to our previous claim that Gpi1-deficient 7B8 cells produce normal amounts of IL-17a, as *in vitro* restimulation was conducted in an artificial microenvironment with strong stimuli, whereas *Il17a*$^{GFP/+}$ reporter cells report the true cytokine production in real physiological conditions. Collectively, these data suggest that Gpi1 is selectively required by the inflammatory encephalitogenic and colitogenic Th17 cells, but not by homeostatic SFB-induced Th17 cells, which differentiated in normal numbers and expressed similar amounts of cytokine as control cells. In contrast, Gapdh, Tpi1 and Ldha are required for the accumulation of both types of Th17 cells.

PPP compensates for Gpi1 deficiency in the homeostatic SFB model

To explain why Gpi1 is unique in selectively impacting the homeostatic SFB model, we hypothesized that the PPP shunt might maintain some glycolytic activity in the *Gpi1* KO cells and thus compensate for Gpi1 deficiency. To determine if metabolites are shunted through the PPP and subsequently re-enter glycolysis upon loss of Gpi1, we performed an *in vitro* isotope tracing experiment. *In vitro* differentiation of Th17 cells can be achieved with combinations of IL-6 and TGF-β, which gives rise to cells lacking EAE pathogenic potential (non-pathogenic Th17, npTh17) (Veldhoen et al., 2006), or IL-6, IL-1β, and IL-23, which mimics the cytokine

bioRxiv preprint doi: https://doi.org/10.1101/857961; this version posted November 29, 2019. The copyright holder for this preprint (which was not certified by peer review) is the author/funder, who has granted bioRxiv a license to display the preprint in perpetuity. It is made available under aCC-BY-NC 4.0 International license.

222 requirement for *in vivo* Th17 cell pathogenicity and programs cells with inflammatory activity
223 (pathogenic Th17, pTh17) (Ghoreschi et al., 2010). Irrespective of the conditions used, *in vitro*
224 differentiated Th17 cells displayed less of a growth defect (25% reduction compared to control
225 *Olfr2* sgRNA) following targeting of *Gpi1* than upon inactivation of *Gapdh* (70% reduction)
226 (Figure 3A). This result resembles the different sensitivities observed in the homeostatic SFB
227 model, suggesting that the cytokine milieu of the pathogenic and homeostatic Th17 cells does
228 not account for the phenotypes of the *Gpi1* mutant mice. We incubated np/p Th17 cells with
229 $^{13}C_{1,2}$-glucose and analyzed downstream ^{13}C label incorporation. The $^{13}C_{1,2}$-glucose tracer is
230 catabolized through glycolysis via Gpi1, producing pyruvate or lactate containing two heavy
231 carbons (M2), while Gpi1-independent shunting through the PPP produces pyruvate and lactate
232 containing one heavy carbon (M1) (Figure 3B) (Lee et al., 1998). Consistent with our hypothesis,
233 we observed ~ 3-fold increase in relative PPP activity in the *Gpi1* KO Th17 cells compared to
234 that in the *Olfr2* KO control, irrespective of npTh17 or pTh17 condition (Figure 3C), indicating
235 that *Gpi1* deficiency maintains active glycolytic flux through PPP shunting.
236 To test whether PPP activity compensates for Gpi1 deficiency *in vivo* in the homeostatic SFB
237 model, we knocked out both *Gpi1* and *G6pdx*, which catalyzes the initial oxidative step in the
238 PPP, with the CRISPR-electroporation transfer system. Combined deletion of these two genes
239 would be expected to block both glycolysis and the PPP, similar to *Gapdh* KO. Consistent with
240 this hypothesis, the *Gpi1/G6pdx* double KO reduced cell number by about 75%, as compared to
241 the co-transferred *Olfr2* KO control cells. This result is in line with our finding that more than
242 60% of cells targeted at two loci have loss of both gene products (Figure S4F). Reduction in the
243 SFB-specific T cells was also significantly different from that observed with inactivation of
244 either *Gpi1* or *G6pdx* alone, but was similar to that with the *Gapdh* single KO (Figure 3D).

bioRxiv preprint doi: https://doi.org/10.1101/857961; this version posted November 29, 2019. The copyright holder for this preprint (which was not certified by peer review) is the author/funder, who has granted bioRxiv a license to display the preprint in perpetuity. It is made available under aCC-BY-NC 4.0 International license.

These results suggest that *in vivo* PPP activity maintains viability of the homeostatic SFB-induced Th17 cells lacking Gpi1.

Increased mitochondrial respiration additionally compensates for Gpi1 deficiency in the homeostatic SFB model

To determine the impact of Gpi1 deficiency on aerobic glycolysis activity, we quantified lactate production by GC-MS and found it to be markedly reduced in *Gpi1* KO cells (Figure 4A). A significant reduction in lactate production may suggest compromised ATP production in *Gpi1* KO cells. As *in vitro* cultured *Gpi1* KO Th17 cells and homeostatic SFB-specific *Gpi1* KO Th17 cells were largely unaffected in terms of cell number and cytokine production, we speculate that there could be an alternative pathway enabling Gpi1-deficient cells to compensate for loss of glycolytic ATP production. We therefore hypothesized that mitochondrial respiration may provide an alternative source of ATP, and measured the oxygen consumption rate (OCR) of *in vitro* cultured *Olfr2* KO control and *Gpi1* KO Th17 cells. Irrespective of npTh17 or pTh17 cell culture condition, there was a significant increase in the ATP-linked respiration rate in *Gpi1* KO compared to *Olfr2* KO control cells (Figures 4B,C)). This suggests that the mitochondria of *Gpi1* KO cells increase their respiration to compensate for the reduction in glycolysis. To evaluate the function of increased respiration with Gpi1 deficiency, we suppressed mitochondrial respiration by treating *in vitro*-cultured Th17 cells with the complex III inhibitor antimycin A. Upon antimycin A treatment, *Gpi1* KO cells were decreased in cell number, similar to *Gapdh*-deficient cells (Figure 4D), consistent with increased mitochondrial respiration compensating for Gpi1 deficiency in the *in vitro* cell culture system.

bioRxiv preprint doi: https://doi.org/10.1101/857961; this version posted November 29, 2019. The copyright holder for this preprint (which was not certified by peer review) is the author/funder, who has granted bioRxiv a license to display the preprint in perpetuity. It is made available under aCC-BY-NC 4.0 International license.

To determine whether increased respiration rescues Gpi1 deficiency *in vivo* in the homeostatic SFB model, we targeted *Gpi1* in 7B8 T cells along with genes responsible for the oxidation of three major substrates feeding the TCA cycle: *Pdha1* (pyruvate), *Gls1* (glutamine), and *Hadhb* (fatty acids). Following co-transfer of control cells and cells lacking either Gpi1 or the mitochondrial enzymes, there was no defect in Th17 cell number, RORγt expression, or cytokine production (data not shown). However, inactivation of both *Gpi1* and *PdhA1* led to a significant reduction in cell number, similar to that with the *Gapdh* KO cells (Figure 4E), suggesting that TCA cycle oxidation of pyruvate compensates for Gpi1 deficiency in homeostatic Th17 cell differentiation induced by SFB colonization.

PPP utilization favors biosynthetic metabolite synthesis in Gpi1-deficient cells

Compensation for *Gpi1* deletion by the PPP and mitochondrial respiration suggests the existence of a partial metabolic redundancy for Gpi1. To understand the compensatory mechanism, we performed kinetic flux profiling, employing GC-MS to measure the passage of isotope label from $^{13}C_6$-glucose into downstream metabolites (Yuan et al., 2008). The resulting kinetic data, along with metabolite abundance, was used to quantify metabolic flux in npTh17 cells prepared from *Gpi1* KO, *Olfr2* KO and cells treated with koningic acid (KA), to inhibit Gapdh (Liberti et al., 2017), since more than 50% of cells in the Gapdh KO culture were WT escapees (Figure S4C)).

Loss of Gpi1 resulted in reduction of glucose uptake (Figure 5A) and in substantially decreased transmission of isotopic label to intracellular pyruvate and lactate, whose abundance was reduced (Figures 5C,D,I). Interestingly, a lower lactate production/glucose consumption ratio was observed in *Gpi1* KO than control cells (Figure 5B), suggesting that Gpi1-deficient cells may be more inclined to use glucose carbons for the synthesis of biosynthetic metabolites,

bioRxiv preprint doi: https://doi.org/10.1101/857961; this version posted November 29, 2019. The copyright holder for this preprint (which was not certified by peer review) is the author/funder, who has granted bioRxiv a license to display the preprint in perpetuity. It is made available under aCC-BY-NC 4.0 International license.

rather than lactate production. Indeed, the labeling rate and total abundance of the biosynthetic metabolites alanine, serine, glycine, and citrate either did not change or were slightly increased in the *Gpi1* KO cells (Figures 5E-I). The flux of pyruvate, lactate, alanine, serine, and glycine in the Gpi1-deficient cells, as compared to *Olfr2* KO control (Figure 5J), was consistent with the PPP supporting the branching pathways of glycolysis important for biosynthetic metabolite production, despite a reduced glycolysis rate.

In contrast, Gapdh inhibition by KA treatment almost completely prevented the synthesis of downstream metabolites (Figures 5C-H). As expected, lactate production was substantially reduced, as shown by an extremely low extracellular acidification rate (ECAR) (Figure 5K). However, unlike the increased mitochondrial activity observed in *Gpi1* KO cells, OCR was not increased upon KA treatment (Figures 5K,L). This effect may be due to the fact that pyruvate oxidation is important for the increased respiration observed in Gpi1-deficient cells and pyruvate production is severely limited in *Gapdh*-deficient cells. Therefore, only basal mitochondrial respiration can be maintained when Gapdh is inhibited.

Taken together, we conclude that the reduced amount of glucose metabolized via the PPP by *Gpi1*-deficient cells was sufficient to support the production of glycolytic intermediates and maintain pyruvate oxidation. *Gpi1*-deficient cells increased their mitochondrial respiration to compensate for the loss of glycolytic flux. In contrast, glycolytic blockade by Gapdh inhibition completely prevented carbon flux needed for key biosynthetic metabolites, which is incompatible with cell viability.

Gpi1 is essential in the hypoxic setting of Th17-mediated inflammation

bioRxiv preprint doi: https://doi.org/10.1101/857961; this version posted November 29, 2019. The copyright holder for this preprint (which was not certified by peer review) is the author/funder, who has granted bioRxiv a license to display the preprint in perpetuity. It is made available under aCC-BY-NC 4.0 International license.

To understand why inflammatory Th17 cells are particularly sensitive to Gpi1 deficiency, we reasoned that metabolic compensation (either through PPP or mitochondrial respiration) upon Gpi1 loss in the homeostatic model is restricted in inflammatory Th17 cells. To address this, we knocked out *G6pdx* in the EAE model, and observed a 70% reduction in 2D2 cell number in the spinal cord (Figures S6A,B), suggesting that PPP flux is required in the setting of inflammation. We therefore sought to understand whether mitochondrial activity is restrained in the inflammatory Th17 cells. Notably, there are a number of reports showing that inflamed tissues, including the spinal cord in EAE and the LILP in colitis, are associated with low oxygenation (hypoxia) (Davies et al., 2013; Johnson et al., 2016; Karhausen et al., 2004; Naughton et al., 1993; Ng et al., 2010; Peters et al., 2004; Van Welden et al., 2017; Yang and Dunn, 2015). As ATP production by respiration requires oxygen as the terminal electron acceptor, we hypothesized that the inflamed spinal cord and LILP are hypoxic to an extent that limits oxygen for mitochondrial respiration. This hypoxia would result in an inability to provide sufficient ATP to compensate for energy loss due to Gpi1 deficiency. To test this hypothesis, we cultured Th17 cells in normoxic (20% O_2) and mild hypoxic (3% O_2) conditions, and found that *Gpi1* KO Th17 cells in the hypoxic state, irrespective of npTh17 or pTh17 differentiation protocols, displayed a growth defect similar to that occurring with Gapdh deficiency (Figure 6A). This result suggests that hypoxia abrogates the compensation from mitochondrial respiration in Gpi1 deficiency.

We next investigated whether the inflamed tissue in the EAE model differs from the homeostatic tissue in the SFB model with regard to oxygen availability. To address this, we performed I.V. injection of pimonidazole, an indicator of O_2 levels, into mice with EAE or with SFB colonization, and found that Th17 cells in the EAE model spinal cord had two-fold higher pimonidazole staining than in the dLN and ~2.7-fold compared to SFB-induced Th17 cells in

bioRxiv preprint doi: https://doi.org/10.1101/857961; this version posted November 29, 2019. The copyright holder for this preprint (which was not certified by peer review) is the author/funder, who has granted bioRxiv a license to display the preprint in perpetuity. It is made available under aCC-BY-NC 4.0 International license.

SILP and mLN (Figure 6B). This result suggests that Th17 cells in the spinal cord of the EAE model experience greater oxygen deprivation than in other tissues examined, including the dLN in the same mice. The increased labeling in the spinal cord was observed in all subsets of $CD4^+$ T cells (Figures S6C,D), indicating that decreased oxygen availability is likely a tissue feature.

Hif1α is an oxygen sensor that is stabilized and activated when cells have limited oxygen availability. Stabilization of Hif1α initiates transcription of its target genes, including glycolysis genes, to allow cells to adapt in poorly oxygenated tissue (Semenza, 2003). To further examine sensitivity to hypoxia in the setting of inflammation, we investigated the effect of *Hif1a* deficiency in the different models of $CD4^+$ T cell differentiation. Using chimeric *Rag1* KO mice reconstituted with equal numbers of $Hif1a^{+/+}CD4^{cre}$ and $Hif1a^{f/f}CD4^{cre}$ bone marrow cells, there was ~ 40% reduction of Hif1α-deficient $CD4^+$ T cells in the spinal cord of mice with EAE, but little difference in the SILP (Figures 6C-E), based on the basal WT/KO total $CD4^+$ T cell number ratio in the peripheral blood before SFB colonization or EAE induction. Furthermore, in the SILP of SFB-colonized mice, there was no significant difference in RORγt and Foxp3 expression or IL-17a and IFN-γ production between WT and KO $CD4^+$ T cells (Figures S6E,F). In contrast, in the spinal cord of the EAE mice, there was a slight decrease in the Th17 cell fractions and increase in the $Foxp3^+$ fraction in the *Hif1a* KO compared to WT $CD4^+$ T cells (Figures S6E, F). Overall, these data suggest that Hif1α is functionally important for the pathogenic Th17 cells (as well as Treg cells) in the EAE model, but not for homeostatic SILP Th17 cells.

To address when and how Gpi1 deficiency impairs inflammatory Th17 cell differentiation and/or function, we performed a time course experiment to assess the kinetics of the co-transferred *Olfr2* KO control and *Gpi1* KO 2D2 cells in the EAE model. *Gpi1* KO T cells, like *Olfr2* KO control cells, were maintained in the dLN until day 13, the last time point when

bioRxiv preprint doi: https://doi.org/10.1101/857961; this version posted November 29, 2019. The copyright holder for this preprint (which was not certified by peer review) is the author/funder, who has granted bioRxiv a license to display the preprint in perpetuity. It is made available under aCC-BY-NC 4.0 International license.

transferred 2D2 cells were still detectable in the dLN (Figure 6E). However, at 13 days post immunization, *Gpi1* mutant cell number was reduced by 50% compared to control T cells in the spinal cord (Figure 6E). This finding is consistent with the previous observation that the spinal cord, but not the dLN, is hypoxic. Accordingly, we observed reduced proliferation of *Gpi1* KO 2D2 cells in the spinal cord but not in the dLN (Figures 6F and S6G). Importantly, 2D2 cells in the dLN of EAE proliferated at a markedly faster rate than 7B8 cells in the mLN of the SFB model (Figures S6H,I). This demonstrates that Gpi1-deficient 2D2 cells can maintain the higher demand for energy and biomass associated with rapid proliferation and emphasizes the role of the SC hypoxic environment in the T cell's dependence on Gpi1. We also examined apoptotis, by staining for the active form of caspase 3, and potential for migration, by staining for Ccr6, and observed no differences between *Gpi1*-deficient and co-transferred *Olfr2* KO control 2D2 T cells (Figures S6J-L). We conclude that the hypoxic environment in the EAE spinal cord impairs mitochondrial respiration, an essential feature for the proliferation and differentiation of Gpi1-deficient T cells. In addition, the results further suggest that T cells overcome the hypoxic environment in the inflamed spinal cord by up-regulating glycolysis, whereas in the homeostatic setting in the SILP they can tolerate reduced glycolytic flux due to higher oxygen levels supporting OXPHOS.

Discussion

Our results demonstrate that *Gpi1,* a glycolysis gene, is selectively required by pathogenic inflammatory Th17 cells but not by homeostatic Th17 cells. We found in both EAE and colitis models that Gpi1 deficiency resulted in the elimination of pathogenic T cells, as observed upon

bioRxiv preprint doi: https://doi.org/10.1101/857961; this version posted November 29, 2019. The copyright holder for this preprint (which was not certified by peer review) is the author/funder, who has granted bioRxiv a license to display the preprint in perpetuity. It is made available under aCC-BY-NC 4.0 International license.

382 inactivation of other glycolysis genes (*Gapdh, Tpi1, Ldha*). However, for homeostatic SFB-
383 specific T cells, *Gpi1* deficiency neither significantly reduced 7B8 cell number, nor impaired
384 their differentiation and IL-17a production, whereas *Gapdh*, *Tpi1*, and *Ldha* mutations resulted
385 in loss of the T cells. Mechanistically, we found that in the homeostatic condition, while *Gapdh*
386 mutation completely blocked flux to distal steps of glycolysis, shunting of carbon through the
387 PPP enabled Gpi-deficient cells to maintain levels of glycolytic intermediates needed for
388 pyruvate oxidation in the TCA cycle and branching pathways that support biomass production.
389 Thus, inactivation of *Gpi1* in the context of the homeostatic model does not impact cell number
390 and cytokine production. In the inflammatory environment, we found that cells are exposed to
391 hypoxia, and as a result cannot increase mitochondrial respiration to compensate for Gpi1
392 deficiency, leading to reduced proliferation and cellularity in the inflammatory tissues. We
393 therefore conclude that *Gpi1* is redundant for the function of homeostatic Th17 cells, but
394 essential in inflammatory Th17 cells. Such selective redundancy suggests not only that Gpi1 can
395 be used as a drug target for hypoxia-related autoimmune diseases, but also that suppressing
396 glycolysis by Gpi1 inhibition could be well tolerated.
397
398 **Glycolysis in CD4$^+$ T cell activation and differentiation**
399 We found that CD4$^+$ T cells (pathogenic or Treg) in the EAE model had greater expression of
400 glycolytic genes than homeostatic CD4$^+$ T cells, which is consistent with the recent
401 demonstration that *Citrobacter*-induced inflammatory Th17 cells were more glycolytic than
402 SFB-induced homeostatic Th17 cells (Omenetti et al., 2019). Our data suggest that T cells adapt
403 to the hypoxic environment in the inflamed spinal cord by up-regulating glycolysis, most likely
404 by hypoxia-stabilized Hif1α.

bioRxiv preprint doi: https://doi.org/10.1101/857961; this version posted November 29, 2019. The copyright holder for this preprint (which was not certified by peer review) is the author/funder, who has granted bioRxiv a license to display the preprint in perpetuity. It is made available under aCC-BY-NC 4.0 International license.

In spite of the difference in glycolytic activity, our *in vivo* genetic data show that blockade of glycolysis is incompatible with Th17 cell activation in either homeostatic or inflammatory models, as *Gapdh* deficiency completely eliminated cells in both models. However, the finding that Gpi1-deficient 2D2 cells proliferated normally in the dLN of the EAE model suggests that T cell activation and differentiation *in vivo* do not necessarily need a fully functional glycolytic pathway. With PPP providing sufficient metabolites for biomass production and mitochondria generating greater amounts of ATP, T cell proliferation and execution of the non-pathogenic Th17 program *in vivo* can be largely maintained in the *Gpi1* KO cells. Our data highlight the complexity of the glycolysis pathway and suggest that not every gene is equally important to glycolytic activity and cell function.

Treg cell differentiation has been proposed to depend on OXPHOS (Kullberg et al., 2006; MacIver et al., 2013; Michalek et al., 2011), and was promoted by glycolysis inhibition *in vitro* with 2DG (Shi et al., 2011). Our *in vivo* genetic data however support an indispensable role of glycolysis in Treg cell differentiation, as demonstrated by complete loss of the intestinal and SC $Foxp3^+$ T cells in mice deficient for *Tpi1* in T cells. In addition, *in vitro* T cell differentiation experiments showed no difference between Treg cells and other effector $CD4^+$ T cells in response to loss of *Gapdh, Gpi1, Ldha*, or *Tpi1*, in terms of cell number and transcription factor expression (data not shown). These data thus suggest that, at the very least, the glycolysis gene *Tpi1* is also essential for iTreg cell differentiation and proliferation.

Gpi1 as a drug target for hypoxia-related diseases

Our study reveals that Gpi1 may be a good drug target for Th17-mediated autoimmune diseases. The sensitivity to Gpi1 deficiency is dependent on whether cells are competent to increase

bioRxiv preprint doi: https://doi.org/10.1101/857961; this version posted November 29, 2019. The copyright holder for this preprint (which was not certified by peer review) is the author/funder, who has granted bioRxiv a license to display the preprint in perpetuity. It is made available under aCC-BY-NC 4.0 International license.

mitochondrial respiration. Therefore, other disease processes involving hypoxia-related pathologies may also be susceptible to Gpi1 inhibition. A recent report showed that 1% O_2 almost completely inhibited *in vitro* growth of *Gpi1*-mutant tumor cell lines, but the proliferation defect was much milder when cells were cultured in normoxic condition (de Padua et al., 2017).This suggests that hypoxia-mediated sensitivity to Gpi1 deficiency can be a general phenomenon, from Th17 cells to tumor cells, which may extend the deployment of Gpi1 inhibition to a broader range of diseases.

Hif1α has been extensively investigated as a drug target in many hypoxia-related pathologies (Bhattarai et al., 2018). As sensitivity to inhibition of both Hif1α and Gpi1 is dependent on oxygen availability, it is of great interest to compare phenotypes of *Hif1a* and *Gpi1* deficiencies in inflammatory conditions. In the mixed bone marrow chimera experiments with the EAE model, there was less than a 2-fold reduction in *Hif1a* mutant compared to wild-type spinal cord $CD4^+$ T cells, whereas *Gpi1*-targeted T cells were reduced 5-fold compared to wild-type cells in the transfer model of EAE. *Hif1a* inactivation efficiency was almost complete (data not shown), while *Gpi1* KO efficiency was roughly 80%, which suggests that Gpi1 deficiency resulted in a more severe defect than *Hif1a* deficiency when the T cells were in a hypoxic environment. This is not unexpected, as Gpi1 itself participates in the glycolysis pathway while Hif1α regulates the transcription of genes in the pathway. Although EAE was attenuated following *Hif1a* inactivation in $CD4^+$ T cells (Dang et al., 2011; Shi et al., 2011), our results suggest that Gpi1 inhibition may be at least as effective a means of blocking cell function in hypoxic microenvironments.

Gpi1 is a targetable glycolysis gene

bioRxiv preprint doi: https://doi.org/10.1101/857961; this version posted November 29, 2019. The copyright holder for this preprint (which was not certified by peer review) is the author/funder, who has granted bioRxiv a license to display the preprint in perpetuity. It is made available under aCC-BY-NC 4.0 International license.

Glycolysis is a universal metabolic pathway whose blockade by inhibitors such as 2DG can yield adverse side effects even at dosages too low to control tumor growth (Raez et al., 2013). 2DG inhibits the first three steps of glycolysis, an effect on glycolysis that is recapitulated by Gapdh inhibition, given that no alternative pathway exists for glucose to enter glycolysis. Although glycolysis is essential for T cell activation, treating diseases caused by autoimmune T cells with drugs that fully inhibit the pathway, e.g. 2DG or KA, would also likely be too toxic at potentially efficacious dosages. In light of the results presented here, Gpi1 may represent a better drug target than other glycolysis gene products for treating Th17 cell-mediated autoimmune diseases. Targeting Gpi1 is conceptually different from general inhibition of glycolysis. Gapdh inhibition and treatment with 2DG are based on the theory that tumor cells or Th17 cells are more glycolytic and hence more sensitive to glycolysis inhibition than healthy or non-inflammatory cells. There is no consideration of compensation in such approach. However, there are multiple cell types heavily reliant on glycolysis, including erythrocytes, neurons and muscle cells that would be also affected by KA or 2DG, resulting in severe side effects. Gpi1 inhibition, by contrast, allows for compensation in the biosynthesis of metabolites and ATP through both PPP and mitochondrial respiration, thus allowing for reduced glycolytic flux in normoxic environments inhabited by homeostatic SFB-induced Th17 cells. This fundamental difference between Gpi1 inhibition and overall glycolysis pathway inhibition raises the possibility that Gpi1 inhibitor concentrations that are sufficiently high to effectively inhibit inflammatory Th17 cells can be tolerated with minimal side effects.

This hypothesis is supported by genetic data obtained from patients with glycolysis gene deficiencies. With few exceptions, patients deficient for *Tpi1* or *Pgk1* have combined symptoms of anemia, mental retardation and muscle weakness [Online Mendelian Inheritance in Man

bioRxiv preprint doi: https://doi.org/10.1101/857961; this version posted November 29, 2019. The copyright holder for this preprint (which was not certified by peer review) is the author/funder, who has granted bioRxiv a license to display the preprint in perpetuity. It is made available under aCC-BY-NC 4.0 International license.

(OMIM) entry 190450, 311800] (Schneider, 2000). Mutations in glycolysis gene products that have redundant isozymes can result in dysfunction of cell types in which only the mutated isozyme gets expressed, such that *Pgam2* deficiency results in muscle breakdown and *Pklr* deficiency causes anemia (Zanella et al., 2005).There have been no *Gapdh* deficiencies reported thus far, suggesting that this enzyme may not even tolerate hypomorphic mutations. The human genetic data are thus consistent with the prediction that inhibition of glycolysis enzymes would result in serious side effects. However, the vast majority of patients with *Gpi1* mutations, which can result in preservation of less than 20% enzymatic activity, have neglectable to severe anemia that is treatable, with no neurological or muscle developmental defects (Baronciani et al., 1996; Kanno et al., 1996; Kugler et al., 1998; McMullin, 1999; Zaidi et al., 2017) [Online Mendelian Inheritance in Man (OMIM) entry 172400]. These clinical data indicate that neurons and muscle cells can afford losing most of their Gpi1 activity even though they require glycolysis, and hence they behave similarly to homeostatic Th17 cells. Collectively, these patient data strongly support our proposal that Gpi1 can be a therapeutic target.

Selective metabolic redundancies permit selective cell inhibition

Metabolic redundancy has been demonstrated in many biological systems, from bacteria to cancer cell lines (Bulcha et al., 2019; Deutscher et al., 2006; Horlbeck et al., 2018; Segre et al., 2005; Thiele et al., 2005; Zhao et al., 2018). Our study demonstrates compensatory metabolic pathways in $CD4^+$ T cells *in vivo*, and highlights that such redundancy can be selective, depending on the cellular microenvironment. Indeed, specific inhibition of pathogenic cells can be achieved by metabolic targeting of selective redundant components. Therefore, characterization of the metabolic redundancy of cells in microenvironments with varying oxygen

bioRxiv preprint doi: https://doi.org/10.1101/857961; this version posted November 29, 2019. The copyright holder for this preprint (which was not certified by peer review) is the author/funder, who has granted bioRxiv a license to display the preprint in perpetuity. It is made available under aCC-BY-NC 4.0 International license.

497 level, pH, abundance of extracellular metabolites, redox status, cytokine milieu, or temperature,
498 may provide opportunities for metabolic targeting of cells in selected tissue microenvironments
499 for therapeutic purposes.
500
501 **Acknowledgements:** We thank the NYU Langone Genome Technology Center for expert
502 library preparation and sequencing. This shared resource is partially supported by the Cancer
503 Center Support Grant P30CA016087 at the Laura and Isaac Perlmutter Cancer Center. We thank
504 Drew R. Jones and Rebecca E. Rose in the NYU Metabolomics Laboratory for helpful
505 discussion and aid with LC-MS data generation and analysis. We thank S.Y. Kim in the NYU
506 Rodent Genetic Engineering Laboratory (RGEL) for generating the Tpi1 conditional KO mice.
507 We thank Anne R. Bresnick (Department of Biochemistry, Albert Einstein College of Medicine)
508 for sharing the S100a4 mutant mice. This work was supported by National Multiple Sclerosis
509 Society Fellowship FG 2089-A-1 (L.W.), by Immunology and Inflammation training grant
510 T32AI100853 (C.N.), by NIH grant R01AI121436 (D.R.L.), by the Howard Hughes Medical
511 Institute (D.R.L.), and the Helen and Martin Kimmel Center for Biology and Medicine (D.R.L.)
512
513
514 **Author Contributions:** L.W. and D.R.L. conceived the project, and wrote the manuscript. L.W.
515 designed, performed experiments, and analyzed the data. K.E.R.H. designed, performed the GC-
516 MS flux, tracing, and seahorse experiments, analyzed the data. Y.H. and R.S. analyzed the
517 scRNAseq data. L.K. analyzed the bulk RNAseq data. C.A., W.L., D.L., and H.M.S. helped with
518 mouse experiments. C.N. and W.L. helped with the development of the CRISPR/Cas9
519 transfection method. S.J. and R.P. helped with GC-MS experiments. K.E.R.H., J.J.L., R.P.,

bioRxiv preprint doi: https://doi.org/10.1101/857961; this version posted November 29, 2019. The copyright holder for this preprint (which was not certified by peer review) is the author/funder, who has granted bioRxiv a license to display the preprint in perpetuity. It is made available under aCC-BY-NC 4.0 International license.

M.E.P., T.Y.P., and A.C.K. assisted with the analysis and interpretation of the metabolic data. K.E.R.H., H.M.S., S.J., J.J.L., R.P., M.E.P., T.Y.P., A.C.K., and R.S. edited the manuscript. D.R.L. supervised the work.

Declaration of Interests: D.R.L. consults and has equity interest in Chemocentryx, Vedanta, and Pfizer Pharmaceuticals.

Figure legends

Figure 1. Encephalitogenic Th17 cells have higher glycolysis pathway gene expression than homeostatic SFB-induced Th17 cells.

(A) Clinical disease course of MOG-CFA-induced EAE in *Tpi1*$^{f/f}$*Cd4*^{cre} (n=7) and *Tpi1*$^{+/+}$*Cd4*^{cre} littermate control mice (n=8). The experiment was repeated twice with the same conclusion. P values were determined using two-way ANOVA, * (P<0.05), **** (P<0.0001).

(B) Heatmap of glycolysis pathway genes expressed in spinal cord Th1*, Th17, and Treg cells in mice with EAE (day 15, score 5) compared to Th17 and Treg cells in the SILP of SFB-colonized mice. Genes are arranged according to the fold change between EAE Th17 and SFB Th17.

(C) Experimental design of the Tpi1 bone marrow reconstitution experiment. Bone marrow cells from *Tpi1*$^{+/+}$ *Cd4*^{cre} CD45.1/2 and *Tpi1*$^{f/f}$ *Cd4*^{cre} CD45.2/2 donor mice were transferred into lethally irradiated CD45.1/1 recipients. Peripheral blood was collected two months later for reconstitution analysis. dLN and SC of the EAE model, and mLN and SILP of the SFB model were dissected at day 15 post EAE induction or SFB colonization.

bioRxiv preprint doi: https://doi.org/10.1101/857961; this version posted November 29, 2019. The copyright holder for this preprint (which was not certified by peer review) is the author/funder, who has granted bioRxiv a license to display the preprint in perpetuity. It is made available under aCC-BY-NC 4.0 International license.

(D,E) Cell number analysis of *Tpi1* WT and KO $CD4^+$ T cells in the SFB model (D) and the EAE model (E). Left panels, representative FACS plots showing the frequencies of the CD45.1/2 and the CD45.2/2 B cells among all B cells in peripheral blood and of the CD45.1/2 and the CD45.2/2 $CD4^+$ T cells among all $CD4^+$ T cells in peripheral blood, mLN or dLN, and SILP of SFB colonized mice or SC of EAE mice. Middle panels, compilation of the cell number ratio of CD45.2/2 to CD45.1/2. Right, normalized KO/WT total $CD4^+$ T cell number ratio in each tissue. The cell number ratio of peripheral B cells was set as 1. P values were determined using paired t tests.

See also Figures S1,2,3.

Figure 2. Gpi1 is selectively required by inflammatory encephalitogenic or colitogenic Th17 cells, but not by homeostatic SFB-induced Th17 cells.

(A) Experimental setup. TCR transgenic Cas9-expressing naïve $CD4^+$ T cells were electroporated with guide amplicons, and co-transferred with *Olfr2* amplicon-electroporated control cells into recipient mice that were immunized for EAE induction (EAE model), or had been colonized with SFB (SFB model) or *Helicobacter hepaticus* (Colitis model).

(B) Representative FACS plots showing the frequencies of *Olfr2* KO cells and the co-transferred glycolytic gene KO cells among total $CD4^+$ T cells in each model.

(C-E) Compilation of cell number ratio of gene KO group to the co-transferred *Olfr2* control for each model, as shown in panel B. The ratio was normalized to *Olfr2*/*Olfr2* co-transfer (*Olfr2*/*Olfr2* cell number ratio was set to 1). Three independent experiments were performed with the same conclusion.

bioRxiv preprint doi: https://doi.org/10.1101/857961; this version posted November 29, 2019. The copyright holder for this preprint (which was not certified by peer review) is the author/funder, who has granted bioRxiv a license to display the preprint in perpetuity. It is made available under aCC-BY-NC 4.0 International license.

(F) Clinical disease course of EAE in *Rag1* KO mice receiving *Olfr2* KO 2D2 cells or *Gpi1* KO 2D2 cells. Experiment was conducted as illustrated in Figure S2C. n=5 mice/group. The experiment was repeated twice with the same conclusion.

(G) Left, representative FACS plot showing RORγt and Foxp3 expression of co-transferred targeted 7B8 cells isolated from the SILP of recipient SFB-colonized mice at day15. Right, ratio of the percentage of RORγt$^+$ Foxp3$^-$ in *Gpi1*- or *Olfr2*-targeted versus co-transferred *Olfr2* control cells in each recipient.

(H) Left, representative FACS histogram showing the overlay of IL17a-GFP expression of co-transferred *Olfr2* KO and *Gpi1* KO 7B8 cells isolated from the SILP of SFB-colonized mice at day15. Right, ratio of the percentage of IL-17a$^+$ cells in *Gpi1*- or *Olfr2*-targeted versus co-transferred *Olfr2* control cells in each recipient.

P values were determined using t tests.

See also Figures S4,5.

Figure 3. PPP activity rescues *Gpi1* deficiency in the homeostatic SFB-induced Th17 cells

(A) Relative number of Th17 cells cultured for 120 h *in vitro*. Naïve Cas9-expressing CD4$^+$ T cells were electroporated with corresponding guide-amplicons and cultured in both npTh17 condition and pTh17 condition. Cell number was normalized to *Olfr2* KO group (*Olfr2* cell number was set as 100). N=3, data are representative of three independent experiments.

(B) Schematic of $^{13}C_{1,2}$-glucose labeling into downstream metabolites. ^{13}C is labeled as filled circle. Catalytic reactions of PPP are labeled as red arrows, while those of glycolysis are in black.

bioRxiv preprint doi: https://doi.org/10.1101/857961; this version posted November 29, 2019. The copyright holder for this preprint (which was not certified by peer review) is the author/funder, who has granted bioRxiv a license to display the preprint in perpetuity. It is made available under aCC-BY-NC 4.0 International license.

(C) Relative PPP activity of *in vitro* cultured Th17 cells. Relative PPP activity from $^{13}C_{1,2}$-glucose was determined using the following equation: PPP= M1/ (M1+M2), where M1 is the fraction of $^{13}C_{1,2}$-glucose derived from the PPP and M2 is the fraction of $^{13}C_{1,2}$-glucose derived from glycolysis. Cells were cultured as in Panel A for 96 h, and medium was changed to isotope-labelled RPMI for 24 h before cell pellets were collected for metabolite extraction.

(D) 7B8 Cas9 transgenic naïve $CD4^+$ T cells were electroporated with a mixture of two guide amplicons (for double KO) before being transferred into recipient mice. Left, representative FACS plots showing the frequencies of co-transferred *Olfr2/Olfr2* control $CD4^+$ T cells and the indicated gene KO $CD4^+$ T cells in the SILP of the SFB model. Right, compilation of cell number ratios of the indicated gene KO combinations to the co-transferred *Olfr2/Olfr2* control. Two independent experiments were performed with same conclusion.

P values were determined using t tests.

Figure 4. Mitochondrial respiration compensates for Gpi1 deficiency in the homeostatic SFB Th17 cells

(A) Lactate secretion of *in vitro* cultured *Olfr2* and *Gpi1* KO np/p Th17 cells. Cells were cultured as in Figure 3A. At 96 h cells were re-plated in new wells with fresh RPMI medium with 10% dialyzed FCS, and supernatants were collected 12 h later for lactate quantification by GC-MS.

(B) Seahorse experiment showing the oxygen consumption rate (OCR) of *in vitro* cultured Th17 cells at baseline and in response to oligomycin (Oligo), carbonyl cyanide 4-(trifluoromethoxy) phenylhydrazone (FCCP), and rotenone plus antimycin (R + A). 10

bioRxiv preprint doi: https://doi.org/10.1101/857961; this version posted November 29, 2019. The copyright holder for this preprint (which was not certified by peer review) is the author/funder, who has granted bioRxiv a license to display the preprint in perpetuity. It is made available under aCC-BY-NC 4.0 International license.

610 replicates were used for the npTh17 *Olfr2* and *Gpi1* targeted cells, 7 replicates for the pTh17
611 *Olfr2*, and 6 replicates for the pTh17 *Gpi1* sets of targeted cells.
612 (C) ATP linked respiration rate quantified based on experiments in panel (B). Representative
613 data from three independent experiments.
614 (D) Relative number of Th17 cells cultured for 120 h *in vitro* (as in Figure 3A), in the presence or
615 absence of 10 nM antimycin A. Cell number was normalized to control (*Olfr2*-targeted cell
616 number was set as 100). n=3, data are representative of two independent experiments.
617 (E) 7B8 Cas9 naïve $CD4^+$ T cells were electroporated with a mixture of two guide amplicons (for
618 double KO) before transfer into recipient mice. Left, representative FACS plots showing the
619 frequencies of co-transferred *Olfr2/Olfr2* control and indicated gene KO $CD4^+$ T cells in the
620 SILP of the SFB model at day 15. Right, compilation of cell number ratios of glycolysis gene
621 KO group to the co-transferred *Olfr2/Olfr2* control. Three independent experiments were
622 performed with same conclusion.
623 P values were determined using t tests.
624
625 **Figure 5. PPP supports normal biomass synthesis in the *Gpi1*-deficient npTh17 cells**
626 *Olfr2*- or *Gpi1*-targeted npTh17 cells (cultured for 96 h as in Figure 3A) were collected for
627 further metabolic analysis.
628 (A, B) Cells were re-plated in U-$^{13}C_6$-glucose tracing medium to measure (A) glucose
629 consumption rate, and (B) ratio of released lactate to consumed glucose by LC-MS.
630 (C-H) Cells were re-plated in U-$^{13}C_6$-glucose tracing medium, and cell pellets were collected at
631 different time points to measure ^{13}C incorporation kinetics of pyruvate (C), lactate (D), serine

bioRxiv preprint doi: https://doi.org/10.1101/857961; this version posted November 29, 2019. The copyright holder for this preprint (which was not certified by peer review) is the author/funder, who has granted bioRxiv a license to display the preprint in perpetuity. It is made available under aCC-BY-NC 4.0 International license.

(E), glycine (F), alanine (G) and citrate (H) in *Olfr2* KO, *Gpi1* KO, or koningic acid (KA)-treated npTh17 cells by GC-MS.

(I) Intracellular abundance of pyruvate, lactate, alanine, serine, glycine and citrate in targeted npTh17 cells, as determined by GC-MS. Raw ion counts were normalized to extraction efficiency and cell number. The abundance is shown relative to the *Olfr2* sample set as 100.

(J) Quantification of the production flux of serine, glycine, alanine, pyruvate and lactate based on the ^{13}C incorporation kinetics and intracellular abundance of each metabolite. Three replicates for each sample.

(K) OCR (top) and ECAR (bottom) of targeted or KA-treated npTh17 cells at baseline and in response to oligomycin (Oligo), carbonyl cyanide 4-(trifluoromethoxy) phenylhydrazone (FCCP), and rotenone plus antimycin (R + A). 10 replicates for each condition.

(L) ATP-linked respiration rate, quantified based on panel K. Data are representative of two independent experiments.

P values were determined using t tests.

Figure 6. Hypoxia in the inflamed spinal cord of the EAE model restrains mitochondrial respiration, leading to the elimination of Gpi1-deficient Th17 cells

(A) Relative number of gRNA-targeted Th17 cells cultured for 120 h *in vitro* in either normoxic (20% O_2) or hypoxic (3% O_2) conditions. Cell number was normalized to *Olfr2* KO (*Olfr2* cell number was set as 100).

(B) Representative FACS histogram showing pimonidazole labeling of total $CD4^+$ T cells isolated from the SC and the dLN at day 15 after induction of EAE and from the SILP and the mLN of SFB-colonized mice.

bioRxiv preprint doi: https://doi.org/10.1101/857961; this version posted November 29, 2019. The copyright holder for this preprint (which was not certified by peer review) is the author/funder, who has granted bioRxiv a license to display the preprint in perpetuity. It is made available under aCC-BY-NC 4.0 International license.

(C) Experimental design of the Hif1a bone marrow reconstitution experiment. *Rag1* KO mice were lethally irradiated and reconstituted with equal numbers of bone marrow cells from *Hif1a*$^{+/+}$ *Cd4*^{cre} CD45.1/2 and *Hif1a*$^{f/f}$ *Cd4*^{cre} CD45.1/1 donors. CD4^{+} T cells were examined 2-months later in peripheral blood (PB), after which mice were either gavaged with SFB or immunized for EAE induction, and CD4^{+} T cells from SC or SILP from each model were isolated at day15 for examination.

(D) Top, representative FACS plots showing the frequencies of *Hif1a*$^{+/+}$ *Cd4*^{cre} and *Hif1a*$^{f/f}$*Cd4*^{cre} CD4^{+} T cells in the peripheral blood and the SILP or the SC of the SFB and the EAE models, respectively. Bottom, compilation of the KO/WT total CD4^{+} cell number ratio obtained in the PB and the SILP or the SC of the SFB and EAE models. Two experiments were performed with the same conclusion.

(E) Time-course of 2D2 cas9 co-transfer experiment. Left, representative FACS plot showing the frequencies of the *Olfr2* control and the co-transferred *Olfr2* or *Gpi1* KO 2D2 cells in total CD4^{+} T cells isolated from the dLN or the SC at different time points of EAE. Right, compilation of the KO/Olfr2 control cell number ratio in the dLN or the SC. Data are representative of two independent experiments.

(F) EDU in vivo labeling of co-transferred 2D2 cells in the EAE model. Left, representative FACS plots showing the frequencies of EDU^{+} among co-transferred *Olfr2* control and *Gpi1* KO 2D2 cells in the SC at the onset of EAE (day10). Middle, compilation of the percentage EDU^{+} cells in the *Olfr2* control and the *Gpi1* KO cells. Right, the *Gpi1* KO/*Olfr2* control ratios of percentage EDU^{+} cells. Two experiments were performed with the same conclusion.

P values were determined using t tests. Panel D, F, and Day13 dLN and SC comparison in panel E were analyzed with paired t tests.

bioRxiv preprint doi: https://doi.org/10.1101/857961; this version posted November 29, 2019. The copyright holder for this preprint (which was not certified by peer review) is the author/funder, who has granted bioRxiv a license to display the preprint in perpetuity. It is made available under aCC-BY-NC 4.0 International license.

See also Figure S6.

STAR Methods

LEAD CONTACT AND MATERIALS AVAILABILITY

Further information and requests for resources and reagents should be directed to and will be fulfilled by the Lead Contact, Dan R. Littman (Dan.Littman@med.nyu.edu).

This study did not generate new unique reagents.

EXPERIMENTAL MODEL AND SUBJECT DETAILS

Mouse Strains

C57BL/6 mice were obtained from Taconic Farms or the Jackson Laboratory. All transgenic animals were bred and maintained in the animal facility of the Skirball Institute (NYU School of Medicine) in specific-pathogen-free (SPF) conditions. *Il-23r*^{GFP} mice (Awasthi et al., 2009) were provided by M. Oukka. *S100a4* knockout mice (Li et al., 2010) were provided by Dr. Anne R. Bresnick. *Cas9*^{Tg} mice (Platt et al., 2014) were obtained from Jackson Laboratory (JAX; B6J.129(Cg)-Gt(ROSA)26Sortm1.1(CAG-cas9*,-EGFP)Fezh/J), and maintained on the Cd45.1 background (JAX; B6. SJL-Ptprca Pepcb/BoyJ). SFB-specific TCRTg (7B8) mice (Yang et al., 2014), MOG-specific TCRTg (2D2) mice (Bettelli et al., 2003), and *Helicobacter hepaticus*-specific TCRTg (HH7-2) mice (Xu et al., 2018) were previously described. They were crossed to the Cas9^{Tg} Cd45.1/1 mice to generate 7B8 *Cas9*^{Tg}, 2D2 *Cas9*^{Tg}, and HH7-2 *Cas9*^{Tg} mice with either Cd45.1/1 or Cd45.1/2 congenic markers. 7B8 Cas9 CD45.1/2 mice were further crossed with *IL17a*$^{GFP/GFP}$ reporter mice (JAX; C57BL/6-Il17atm1Bcgen/J) to generate 7B8 *Cas9*

bioRxiv preprint doi: https://doi.org/10.1101/857961; this version posted November 29, 2019. The copyright holder for this preprint (which was not certified by peer review) is the author/funder, who has granted bioRxiv a license to display the preprint in perpetuity. It is made available under aCC-BY-NC 4.0 International license.

IL17a$^{GFP/+}$ Cd45.1/2 or Cd45.2/2 mice. Female *Foxp3*$^{RFP/RFP}$ reporter mice (Jax; C57BL/6-Foxp3^{tm1Flv}/J) were crossed with male *IL17a*$^{GFP/GFP}$ reporter mice to generate *IL17a*$^{GFP/+}$ *Foxp3*^{RFP} male mice for bulk RNAseq. *Hif1a*$^{f/f}$ mice (Jax; B6.129-Hif1a^{tm3Rsjo}/J) were crossed with *CD4*^{cre} mice (Jax; B6.Cg-Tg(Cd4-cre)1Cwi/BfluJ) and CD45.1/1 mice to generate *Hif1a*$^{+/+}$ *CD4*^{cre} CD45.1/1 and *Hif1a*$^{f/f}$ *CD4*^{cre} CD45.2/2 littermates. *Tpi1*$^{f/+}$ mice generated by crossing *Tpi1*$^{tm1a(EUCOMM)Wtsi}$ mice (Wellcome Trust Sanger Institute; B6Brd;B6N-Tyr^{c-Brd} Tpi1$^{tm1a(EUCOMM)Wtsi}$/WtsiCnbc) with a FLP deleter strain (Jax; B6.129S4-Gt(ROSA)26Sor$^{tm1(FLP1)Dym}$/RainJ) were further crossed with CD4^{cre} and CD45.1/1 strains to generate *Tpi1*$^{+/+}$*Cd4*^{cre} and *Tpi1*$^{f/f}$*CD4*^{cre} mice with different congenic markers.

METHOD DETAILS

Flow cytometry

For transcription factor and cytokine staining of *ex vivo* cells, single cell suspensions were incubated for 3h in RPMI with 10% FBS, phorbol 12-myristate 13-acetate (PMA) (50 ng/ml; Sigma), ionomycin (500 ng/ml;Sigma) and GolgiStop (BD). Cells were then resuspended with surface-staining antibodies in HEPES-buffered HBSS. Staining was performed for 20-30 min on ice. Surface-stained cells were washed and resuspended in live/dead fixable blue (ThermoFisher) for 5 min prior to fixation. Cells were treated using the FoxP3 staining buffer set from eBioscience according to the manufacturer's protocol. Intracellular stains were prepared in 1X eBioscience permwash buffer containing anti-CD16/anti-CD32, normal mouse IgG, and normal rat IgG Staining was performed for 30-60 min on ice.

bioRxiv preprint doi: https://doi.org/10.1101/857961; this version posted November 29, 2019. The copyright holder for this preprint (which was not certified by peer review) is the author/funder, who has granted bioRxiv a license to display the preprint in perpetuity. It is made available under aCC-BY-NC 4.0 International license.

723 For cytokine analysis of *in vitro* cultured Th17 cells, cells were incubated in the restimulation
724 buffer for 3 h. After surface and live/dead staining, cells were treated using the
725 Cytofix/Cytoperm buffer set from BD Biosciences according to the manufacturer's protocol.
726 Intracellular stains were prepared in BD permwash in the same manner used for transcription
727 factor staining. Flow cytometric analysis was performed on an LSR II (BD Biosciences) or an
728 Aria II (BD Biosciences) and analyzed using FlowJo software (Tree Star).
729

730 **Retroviral transduction and 2D2 TCRtg Cas9^{Tg} T cell-mediated EAE**

731 sgRNAs were designed using the Crispr guide design software (http://crispr.mit.edu/). sgRNA
732 encoding sequences were cloned into the retroviral sgRNA expression vector pSIN-U6-
733 sgRNAEF1as-Thy1.1-P2A-Neo that has been reported before (Ng et al., 2019). To make the
734 double sgRNA vector for experiments shown in Figures S2A-D, the sgRNA transcription
735 cassette, ranging from the U6 promoter to the U6 terminator, was amplified and cloned into the
736 pSIN vector after the first sgRNA encoding cassette. Retroviruses were packaged in PlatE cells
737 by transient transfection using TransIT 293 (Mirus Bio).
738

739 Tissue culture plates were coated with polyclonal goat anti-hamster IgG (MP Biomedicals) at
740 37 °C for at least 3 h and washed 3× with PBS before cell plating. FACS-sorted
741 $CD4^+CD8^-CD25^-CD62L^+CD44^{low}$ naïve 2D2 TCRtg *Cas9^{Tg}* T cells were seeded for 24 h in T
742 cell medium (RPMI supplemented with 10% FCS, 2mM□□-mercaptoethanol, 2mM
743 glutamine), along with anti-CD3 (BioXcell, clone 145-2C11, 0.25µg/ml) and anti-CD28
744 (BioXcell, clone 37.5.1, 1µg/ml) antibodies. Cells were then transduced with the pSIN virus
745 by spin infection at 1200 × g at 30 °C for 90 min in the presence of 10µg/ml polybrene

bioRxiv preprint doi: https://doi.org/10.1101/857961; this version posted November 29, 2019. The copyright holder for this preprint (which was not certified by peer review) is the author/funder, who has granted bioRxiv a license to display the preprint in perpetuity. It is made available under aCC-BY-NC 4.0 International license.

(Sigma). Viral supernatants were removed 12 h later and replaced with fresh medium containing anti-CD3/anti-CD28, 20ng/ml IL-6 and 0.3ng/ml TGF-□. Cells were lifted off 48 h later and supplemented with IL-2 for another 48hours. Thy1.1^{high} cells were then sorted with the ARIA and i.v. injected into *Rag1*$^{-/-}$ mice (50k cells/mouse). Mice were then immunized subcutaneously on day 0 with 100µg of MOG_{35-55} peptide, emulsified in CFA (Complete Freund's Adjuvant supplemented with 2mg/mL *Mycobacterium tuberculosis* H37Ra), and injected i.p. with 200 ng pertussis toxin (Calbiochem). The EAE scoring system was as follows: 0-no disease, 1-Partially limp tail; 2-Paralyzed tail; 3-Hind limb paresis, uncoordinated movement; 4-One hind limb paralyzed; 5-Both hind limbs paralyzed; 6-Hind limbs paralyzed, weakness in forelimbs; 7-Hind limbs paralyzed, one forelimb paralyzed; 8-Hind limbs paralyzed, both forelimbs paralyzed; 9-Moribund; 10-Death.

sgRNA guide amplicon electroporation of naïve CD4$^+$ T cells

sgRNA-encoding sequences were cloned into the pSIN vector (single sgRNA in one vector). The sgRNA encoding cassette, ranging from the U6 promoter to the U6 terminator, was amplified with 34 cycles of PCR with Phusion (NEB), and purified with Wizard SV Gel and PCR Clean-up System (Promega), and concentrated with a standard ethanol DNA precipitation protocol. Amplicons were resuspended in a small volume of H_2O and kept at -80 °C until use. Amplicon concentration was measured with Qubit dsDNA HS assay kit (Thermofisher)

The Amaxa P3 Primary Cell 4D-Nucleofector X kit was used for T cell electroporation. 2 million FACS-sorted naïve CD4$^+$ *Cas9*^{Tg} cells were pelleted and resuspended in 100ul P3

bioRxiv preprint doi: https://doi.org/10.1101/857961; this version posted November 29, 2019. The copyright holder for this preprint (which was not certified by peer review) is the author/funder, who has granted bioRxiv a license to display the preprint in perpetuity. It is made available under aCC-BY-NC 4.0 International license.

769 primary cell solution supplemented with 0.56ug sgRNA amplicon (for single gene knockout),
770 or equal amounts of sgRNA amplicons (0.56ug each for targeting two genes simultaneously in
771 Figures 3D, and 4E). Cell suspensions were transferred into a Nucleocuvette Vessel for
772 electroporation in the Nucleofector X unit, using program "T cell. Mouse. Unstim.". Cells
773 were then rested in 500 □l mouse T cell nucleofector medium (Lonza) for 30 min before in
774 vitro culture or transfer into mice.
775
776 In vitro cell culture – 96 well flat-bottom tissue culture plates (Corning) were coated with
777 polyclonal goat anti-hamster IgG (MP Biomedicals) at 37 °C for at least 3 h and washed 3×
778 with PBS before cell plating. Electroporated cells were plated into each well containing 200ul
779 T cell culture medium (glucose-free RPMI (ThermoFisher) supplemented with 10% FCS
780 (Atlanta Biologicals), 4g/L glucose, 4mM glutamine, 50uM □-mercaptoethanol, 0.25μg/ml
781 anti-CD3 (BioXcell, clone 145-2C11) and 1μg/ml anti-CD28 (BioXcell, clone 37.5.1)
782 antibodies). For npTh17 culture, 20ng/ml IL-6 and 0.3ng/ml TGF-□ were further added into
783 the T cell medium. For pTh17 cell culture, 20ng/ml IL-6, 20ng/ml IL-23, and 20ng/ml IL-1□
784 were further added into the T cell medium. Cells were then cultured for 96 h or 120 h before
785 metabolic experiments or cell number counting/western/FACS profiling, respectively.
786
787 T cell transfer into mice – TCR transgenic *Cas9*^{Tg} naïve CD4^{+} T cells (7B8 TCRtg for SFB
788 model, 2D2 TCRtg for EAE model, and HH7-2 TCRtg for colitis model) with different
789 isotype markers were electroporated at the same time. Equal numbers of isotype-distinct
790 electroporated resting cells were mixed, pelleted and resuspended in dPBS supplemented with
791 1% filtered FBS before retro-orbital injection into recipient mice (100,000 cells in total for

bioRxiv preprint doi: https://doi.org/10.1101/857961; this version posted November 29, 2019. The copyright holder for this preprint (which was not certified by peer review) is the author/funder, who has granted bioRxiv a license to display the preprint in perpetuity. It is made available under aCC-BY-NC 4.0 International license.

each mouse). The transferred cells were isolated from SILP of the SFB model, SC of the EAE model, and the LILP of the colitis model at day 15 post transfer, unless otherwise indicated.

SFB model

C57BL/6 mice were purchased from Jackson Laboratory and maintained in SFB-free SPF cages. Fresh feces of SFB mono-colonized mice maintained in our gnotobiotic animal facility were collected and frozen at -80 °C until use. Fecal pellets were meshed through a 100uM strainer (Corning) in cold sterile dPBS (Hyclone). 300 □l feces suspension, equal to the amount of 1/3 pellet, was administered to each mouse by oral gavage. Mice were inoculated one more time at 24 h. For the transfer experiment, electroporated cells were injected 96 h after the initial gavage.

Colitis model

H. hepaticus was provided by J. Fox (MIT) and grown on blood agar plates (TSA with 5% sheep blood, Thermo Fisher) as previously described (Xu et al., 2018). Briefly, *Rag1*$^{-/-}$ mice were colonized with *H. hepaticus* by oral gavage on days 0 and 4 of the experiment. At day 7, electroporated naïve HH7-2 TCRtg *Cas9*^{Tg} CD4^{+} T cells were adoptively transferred into the *H. hepaticus*-colonized recipients. In order to confirm *H. hepaticus* colonization, *H. hepaticus*-specific 16S primers were used on DNA extracted from fecal pellets. Universal 16S were quantified simultaneously to normalize *H. hepaticus* colonization of each sample.

EAE model

Right after the transfer of electroporated 2D2 *Cas9*^{Tg} cells, mice were immunized subcutaneously on day 0 with 100μg of MOG_{35-55} peptide, emulsified in CFA (Complete Freund's Adjuvant

bioRxiv preprint doi: https://doi.org/10.1101/857961; this version posted November 29, 2019. The copyright holder for this preprint (which was not certified by peer review) is the author/funder, who has granted bioRxiv a license to display the preprint in perpetuity. It is made available under aCC-BY-NC 4.0 International license.

supplemented with 2mg/mL Mycobacterium tuberculosis H37Ra), and injected i.p. on days 0 and 2 with 200 ng pertussis toxin (Calbiochem).

Isolation of lymphocytes from lamina propria, spinal cord, and lymph nodes

For isolating mononuclear cells from the lamina propria, the intestine (small and/or large) was removed immediately after euthanasia, carefully stripped of mesenteric fat and Peyer's patches/cecal patch, sliced longitudinally and vigorously washed in cold HEPES buffered (25mM), divalent cation-free HBSS to remove all fecal traces. The tissue was cut into 1-inch fragments and placed in a 50ml conical containing 10ml of HEPES buffered (25mM), divalent cation-free HBSS and 1 mM of fresh DTT. The conical was placed in a bacterial shaker set to 37 °C and 200rpm for 10 minutes. After 45 seconds of vigorously shaking the conical by hand, the tissue was moved to a fresh conical containing 10ml of HEPES buffered (25mM), divalent cation-free HBSS and 5 mM of EDTA. The conical was placed in a bacterial shaker set to 37 °C and 200rpm for 10 minutes. After 45 seconds of vigorously shaking the conical by hand, the EDTA wash was repeated once more in order to completely remove epithelial cells. The tissue was minced and digested in 5-7ml of 10% FBS-supplemented RPMI containing collagenase (1 mg/ml collagenaseD; Roche), DNase I (100 µg/ml; Sigma), dispase (0.05 U/ml; Worthington) and subjected to constant shaking at 155rpm, 37 °C for 35 min (small intestine) or 55 min (large intestine). Digested tissue was vigorously shaken by hand for 2 min before adding 2 volumes of media and subsequently passed through a 70 µm cell strainer. The tissue was spun down and resuspended in 40% buffered percoll solution, which was then aliquoted into a 15ml conical. An equal volume of 80% buffered percoll solution was underlaid to create a sharp interface. The

bioRxiv preprint doi: https://doi.org/10.1101/857961; this version posted November 29, 2019. The copyright holder for this preprint (which was not certified by peer review) is the author/funder, who has granted bioRxiv a license to display the preprint in perpetuity. It is made available under aCC-BY-NC 4.0 International license.

tube was spun at 2200rpm for 22 min at 22 °C to enrich for live mononuclear cells. Lamina propria (LP) lymphocytes were collected from the interface and washed once prior to staining.

For isolating mononuclear cells from spinal cords during EAE, spinal cords were mechanically disrupted and dissociated in RPMI containing collagenase (1 mg/ml collagenaseD; Roche), DNase I (100 µg/ml; Sigma) and 10% FBS at 37 °C for 30 min. Leukocytes were collected at the interface of a 40%/80% Percoll gradient (GE Healthcare).

For isolating mononuclear cells from lymph nodes, mesenteric lymph nodes (for the SFB model), and draining lymph nodes (Inguinal, axillary, and brachial lymph nodes for the EAE model) were mechanically dissected and minced in RPMI containing 10% FBS and 25mM HEPES through 40uM strainer. Cells were collected for further analysis.

Generation of bone marrow chimeric reconstituted mice

Bone marrow mononuclear cells were isolated from donor mice by flushing the long bones. To generate *Tpi1*^{WT}/ *Tpi1*^{KO} chimeric reconstituted mice, *Tpi1*$^{+/+}$ *Cd4*^{Cre} CD45.1/2 and *Tpi1*$^{f/f}$ *Cd4*^{Cre} CD45.2/2 mice were used as donors. To generate *Hif1a*^{WT}/*Hif1a*^{KO} chimeric reconstituted mice, *Hif1a*$^{+/+}$ *Cd4*^{Cre} CD45.1/2 and *Hif1a*$^{f/f}$ *Cd4*^{Cre} CD45.1/1 mice were used as donors. To generate *Il23r*^{het}/*Il23r*^{KO} chimeric reconstituted mice, *Il23r*$^{Gfp/+}$ CD45.1/2 *and Il23r*$^{Gfp/Gfp}$ CD45.1/1 mice were used as donors. Red blood cells were lysed with ACK Lysing Buffer, and CD4/CD8 T cells were labeled with CD4/CD8 magnetic microbeads and depleted with a Miltenyi LD column. The remaining cells were resuspended in PBS for injection in at a 1:1 ratio (WT: KO). 4×10^6 cells were injected intravenously into 6 week old mice (CD45.1/1 in Tpi1 experiment; Rag1$^{-/-}$ in Hif1a experiment) that were irradiated 4h before reconstitution using 1000 rads/mouse (2x500rads, at an interval of 3h, at X-RAD 320 X-Ray Irradiator). Peripheral blood samples

bioRxiv preprint doi: https://doi.org/10.1101/857961; this version posted November 29, 2019. The copyright holder for this preprint (which was not certified by peer review) is the author/funder, who has granted bioRxiv a license to display the preprint in perpetuity. It is made available under aCC-BY-NC 4.0 International license.

were collected and analyzed by FACS 8 weeks later to check for reconstitution, after which SFB colonization or EAE induction were performed.

Pimonidazole HCl labeling

Pimonidazole HCl (hypoxyprobe) was retro orbitally injected into mice at the dose of 100mg/kg under general anesthesia (Ketamine 100mg/Kg, Xylazine 15mg/Kg). 3 h later, tissues were dissected and processed to get the mononuclear cell fraction. After surface/live/dead staining, cells were treated using the FoxP3 staining buffer set from eBioscience according to the manufacturer's protocol. Intracellular staining with anti-RORγt, Foxp3, Tbet, and biotin-pimonidazole adduct antibodies were performed for 60min on ice in 1X eBioscience permwash buffer containing normal mouse IgG (50μg/ml), and normal rat IgG (50μg/ml). The pimonidazole labeling was visualized with streptavidin APC staining in the same buffer.

EdU incorporation

Two doses of EdU (50mg/kg for each) were i.p. injected into MOG/CFA-immunized mice in 12 h intervals at days 4, 6, 8, 9, and 12 post immunization. Draining lymph nodes and/or spinal cords were dissected 12 h post the second injection. Detection of EdU incorporation into the DNA was performed with EdU-click 647 Kit (Baseclick) according to the manufacturer's instructions. In brief, surface-stained cells were fixed in 100μl fixative solution, and permeabilized in 100μl permeabilization buffer. Cells were pelleted and incubated for 30min in 220μl EdU reaction mixture containing 20μl permeabilization buffer, 20μl buffer additive, 1μl dye azide, 4μl catalyst solution, and 175μl dPBS, before 3x wash and FACS analysis.

bioRxiv preprint doi: https://doi.org/10.1101/857961; this version posted November 29, 2019. The copyright holder for this preprint (which was not certified by peer review) is the author/funder, who has granted bioRxiv a license to display the preprint in perpetuity. It is made available under aCC-BY-NC 4.0 International license.

883 **CFSE labeling**

884 Sorted naïve 7B8 or 2D2 CD45.1/1 CD4 T cells were stained with CFSE cell proliferation kit
885 (Life Technology). Labeled cells were administered into each congenic CD45.2/2 recipient
886 mouse by retro-orbital injection. Mice receiving 7B8 cells were gavaged with SFB mono-feces
887 twice on days -4 and -3. Mice receiving 2D2 cells were immunized for EAE induction
888 immediately after cell transfer. mLNs of the SFB-colonized mice were collected at 72h and
889 120h, and dLN of 2D2-injected mice were collected at 72h, 96h and 120h post transfer for cell
890 division analysis.

891

892 **Bulk RNA sequencing**

893 Total RNA from sorted target cell populations was isolated using TRIzol LS (Invitrogen)
894 followed by DNase I (Qiagen) treatment and cleanup with RNeasy Plus Micro kit (Qiagen;
895 74034). RNA quality was assessed using Pico Bioanalyser chips (Agilent). RNASeq libraries
896 were prepared using the Clontech Smart-Seq Ultra low RNA kit (Takara Bio) for cDNA
897 preparation, starting with 550 pg of total RNA, and 13 cycles of PCR for cDNA amplification.
898 The SMARTer Thruplex DNA-Seq kit (Takara Bio) was used for library prep, with 7 cycles of
899 PCR amplification, following the manufacturer's protocol. The amplified library was purified
900 using AMPure beads (Beckman Coulter), quantified by Qubit and QPCR, and visualized in an
901 Agilent Bioanalyzer. The libraries were pooled equimolarly, and run on a HiSeq 4000, as paired
902 end reads, 50 nucleotides in length.

903

904 **Single cell RNAseq**

bioRxiv preprint doi: https://doi.org/10.1101/857961; this version posted November 29, 2019. The copyright holder for this preprint (which was not certified by peer review) is the author/funder, who has granted bioRxiv a license to display the preprint in perpetuity. It is made available under aCC-BY-NC 4.0 International license.

905 Libraries from isolated single cells were generated based on the Smart-seq2 protocol (Picelli et
906 al., 2014) with the following modifications. In brief, RNA from sorted single cells was used as
907 template for oligo-dT primed reverse transcription with Superscript II Reverse Transcriptase
908 (Thermo Fisher), and the cDNA library was generated by 20 cycle PCR amplification with IS
909 PCR primer using KAPA HiFi HotStart ReadyMix (KAPA Biosystems) followed by Agencourt
910 AMPure XP bead purification (Beckman Coulter) as described. Libraries were tagmented using
911 the Nextera XT Library Prep kit (Illumina) with custom barcode adapters (sequences available
912 upon request). Libraries with unique barcodes were combined and sequenced on a HiSeq2500 in
913 RapidRun mode, with either 2x50 or 1x50 nt reads.
914
915 **Stable-isotope tracing, metabolite secretion and kinetic flux profiling by GC-MS**
916 *In vitro* cultured np/pTh17 cells were collected at 96h, washed twice in glucose-free RPMI
917 (ThermoFisher, 11879020) containing 10% dialyzed FBS (ThermoFisher), and re-plated in anti-
918 hamster IgG-coated 96-well plates at 60,000/well in np/pTh17 medium (glucose-free RPMI
919 containing 10% dialyzed FBS, 2mM □-mercaptoethanol, 4mM glutamine, anti-CD3, anti-
920 CD28, and 4g/L isotype labeled glucose). For KA-treated samples, *Olfr2* KO cells were
921 previously treated with 30 μM KA before collection and re-plating. The re-plated cells were
922 cultured in Th17 medium supplemented with 30 μM KA.
923
924 To measure relative PPP activity, $^{13}C_{1,2}$-glucose (Cambridge Isotope Laboratories) was added
925 into the Th17 medium. Re-plated cells were further cultured 12 h before metabolite extraction
926 and GC-MS analysis. After a brief wash with 0.9% ice-cold saline solution to remove media
927 contamination, cellular metabolites were extracted using a pre-chilled

bioRxiv preprint doi: https://doi.org/10.1101/857961; this version posted November 29, 2019. The copyright holder for this preprint (which was not certified by peer review) is the author/funder, who has granted bioRxiv a license to display the preprint in perpetuity. It is made available under aCC-BY-NC 4.0 International license.

methanol/water/chloroform extraction method, as previously described (Metallo et al., 2011). Aqueous and inorganic layers were separated by cold centrifugation for 15 min. The aqueous layer was transferred to sample vials (Agilent 5190-2243) and evaporated to dryness using a SpeedVac (Savant Thermo SPD111V).

For lactate secretion analysis, media was collected at 12 h and centrifuged at 1,000 x g to pellet cellular debris. 5 µL of supernatant was extracted in 80% ice-cold methanol mixture containing isotope-labeled internal standards and evaporated to dryness.

Metabolite abundance [X_m] was determined using the following equation:

$$[X_m] = \frac{X_{std} - \%M0_x}{100 - \%M0_x}$$

where X_{std} is the molar amount of isotope-labeled standard (e.g. 5 nmol lactate) and $\%M0_x$ is the relative abundance of unlabeled metabolite X corrected for natural isotope abundance.

To quantify the metabolite secretion flux ($Flux_m$), the molar change in extracellular metabolites was determined by calculating the difference between conditioned and fresh media and normalizing to changes in cell density:

$$Flux_m = \frac{X_f - X_i}{\int_0^f X_0\, e^{kt}}$$

bioRxiv preprint doi: https://doi.org/10.1101/857961; this version posted November 29, 2019. The copyright holder for this preprint (which was not certified by peer review) is the author/funder, who has granted bioRxiv a license to display the preprint in perpetuity. It is made available under aCC-BY-NC 4.0 International license.

where X_f and X_i are the final and initial molar amounts of metabolite, respectively, X_0 is the initial cell density, k is the exponential growth rate (hr^{-1}), and t is the media conditioning time.

For kinetic flux profiling, npTh17 medium was supplemented with 4g/L $^{13}C_6$-glucose (Cambridge Isotope Laboratories). Cells were collected at various time points. Unlabeled metabolite (M0) versus time (t) were plotted and the data were fitted to an equation as previously described (Yuan et al., 2008) to quantify the metabolite turnover rate (t^{-1}):

$$Y = (1 - \alpha)^* \exp(-k^* t) + \alpha$$

where □ is the percentage of unlabeled (M0) metabolite at steady-state, k is the metabolite turnover rate and t is time.

Metabolite flux was quantified by multiplying the decay rate by the intracellular metabolite abundance.

Metabolite derivatization using MOX-tBDMS was conducted as previously described (Lewis et al., 2014). Derivatized samples were analyzed by GC-MS using a DB-35MS column (30m x 0.25mm i.d. x 0.25 µm) installed in an Agilent 7890B gas chromatograph (GC) interfaced with an Agilent 5977B mass spectrometer as previously described (Grassian et al., 2014) and corrected for natural abundance using in-house algorithms adapted from (Fernandez et al., 1996).

LC-MS analysis

bioRxiv preprint doi: https://doi.org/10.1101/857961; this version posted November 29, 2019. The copyright holder for this preprint (which was not certified by peer review) is the author/funder, who has granted bioRxiv a license to display the preprint in perpetuity. It is made available under aCC-BY-NC 4.0 International license.

For glucose consumption analysis, supernatants of npTh17 cells, or cell free control, were collected at 24h post cell re-plating. Metabolites were extracted for LC-MS analysis to measure glucose and lactate quantities. Glucose consumption rate and lactate production rate was quantified on a relative basis by calculating the ion count difference between conditioned and fresh media and normalizing to changes in cell density.

Samples were subjected to an LC-MS analysis to detect and quantify known peaks. A metabolite extraction was carried out on each sample with a previously described method (Pacold et al., 2016). In brief, samples were extracted by mixing 10 µL of sample with 490 µL of extraction buffer (81.63% methanol (Fisher Scientific) and 500 nM metabolomics amino acid mix standard (Cambridge Isotope Laboratories, Inc.)) in 2.0mL screw cap vials containing ~100 µL of disruption beads (Research Products International, Mount Prospect, IL). Each was homogenized for 10 cycles on a bead blaster homogenizer (Benchmark Scientific, Edison, NJ). Cycling consisted of a 30 sec homogenization time at 6 m/s followed by a 30 sec pause. Samples were subsequently spun at 21,000 g for 3 min at 4 °C. A set volume of each (360 µL) was transferred to a 1.5 mL tube and dried down by speedvac (Thermo Fisher, Waltham, MA). Samples were reconstituted in 40 µL of Optima LC/MS grade water (Fisher Scientific, Waltham, MA). Samples were sonicated for 2 mins, then spun at 21,000g for 3min at 4°C. Twenty microliters were transferred to LC vials containing glass inserts for analysis.

The LC column was a MilliporeTM ZIC-pHILIC (2.1 x150 mm, 5 µm) coupled to a Dionex Ultimate 3000TM system and the column oven temperature was set to 25 °C for the gradient elution. A flow rate of 100 µL/min was used with the following buffers; A) 10 mM ammonium

bioRxiv preprint doi: https://doi.org/10.1101/857961; this version posted November 29, 2019. The copyright holder for this preprint (which was not certified by peer review) is the author/funder, who has granted bioRxiv a license to display the preprint in perpetuity. It is made available under aCC-BY-NC 4.0 International license.

carbonate in water, pH 9.0, and B) neat acetonitrile. The gradient profile was as follows; 80-20%B (0-30 min), 20-80%B (30-31 min), 80-80%B (31-42 min). Injection volume was set to 1 µL for all analyses (42 min total run time per injection).

MS analyses were carried out by coupling the LC system to a Thermo Q Exactive HFTM mass spectrometer operating in heated electrospray ionization mode (HESI). Method duration was 30 min with a polarity switching data-dependent Top 5 method for both positive and negative modes. Spray voltage for both positive and negative modes was 3.5kV and capillary temperature was set to 320°C with a sheath gas rate of 35, aux gas of 10, and max spray current of 100 µA. The full MS scan for both polarities utilized 120,000 resolution with an AGC target of 3e6 and a maximum IT of 100 ms, and the scan range was from 67-1000 m/z. Tandem MS spectra for both positive and negative mode used a resolution of 15,000, AGC target of 1e5, maximum IT of 50 ms, isolation window of 0.4 m/z, isolation offset of 0.1 m/z, fixed first mass of 50 m/z, and 3-way multiplexed normalized collision energies (nCE) of 10, 35, 80. The minimum AGC target was 1e4 with an intensity threshold of 2e5. All data were acquired in profile mode.

Seahorse Analysis

OCR and ECAR measurements were performed using a Seahorse XFe96 analyzer (Seahorse Biosciences). Seahorse XFe96 plates were coated with 0.56ug Cell-Tak (Corning) in 24□l coating buffer (8□l H_2O + 16□l 0.1M $NaHCO_3$ (PH 8.0)) overnight at 4 °C, and washed 3x with H_2O before use. *In vitro* cultured Th17 cells were collected at 96 h, washed twice in Seahorse RPMI media PH7.4 (Agilent, 103576-100) and seeded onto the coated plates at 100,000 per well. To measure the OCR and ECAR of KA-treated cells, 30□M KA (Santa Cruz) was added into

bioRxiv preprint doi: https://doi.org/10.1101/857961; this version posted November 29, 2019. The copyright holder for this preprint (which was not certified by peer review) is the author/funder, who has granted bioRxiv a license to display the preprint in perpetuity. It is made available under aCC-BY-NC 4.0 International license.

Olfr2 control Th17 cell samples at the beginning of the Seahorse measurement. Respiratory rates were measured in RPMI Seahorse media, pH7.4 (Agilent) supplemented with 10 mM glucose (Agilent) and 2 mM glutamine (Agilent) in response to sequential injections of oligomycin (1 μM) , FCCP (0.5 μM) and antimycin/rotenone (1 μM) (all Cayman Chemicals, Ann Arbor, MI, USA).

Western blotting

Whole cell extracts were fractionated by SDS-PAGE and transferred to nitrocellulose membrane by wet transfer for 4 h on ice at 60 V. Blots were blocked in TBS blocking buffer (Licor) and then stained overnight with primary antibody at 4°C. The next day, membranes were washed three times in TBST (TBS and 0.1% Tween-20), stained with fluorescently conjugated secondary antibodies (Licor) at 1:10,000 dilution in TBS blocking buffer for 1 h at room temperature, and then imaged in the 680- and 800-nm channels. Antibodies used: Gapdh (CST), Gpi1 (Thermo Fisher), Ldha (CST), Pdha1 (Abcam), Tpi1 (Abcam), G6pdx (Abcam), □-tubulin (Santa Cruz).

QUANTIFICATION AND STATISTICAL ANALYSIS

Bulk RNAseq analysis

Raw reads from bulk RNA-seq were aligned to the mm10 genome using STAR v 2.6.1d with the quantmode parameter to get read counts. DESeq2 v 1.22.2 was used for differential expression analysis. Heatmaps were produced using gplots v 3.0.1.1.

Pre-processing of scRNA-seq data

bioRxiv preprint doi: https://doi.org/10.1101/857961; this version posted November 29, 2019. The copyright holder for this preprint (which was not certified by peer review) is the author/funder, who has granted bioRxiv a license to display the preprint in perpetuity. It is made available under aCC-BY-NC 4.0 International license.

1041 The single cell RNA raw sequence reads were aligned to the UCSC Mus musculus genome,
1042 mm10, using Kallisto (Bray et al., 2016). The mean number of reads per cell was 241,500. Gene
1043 expression values were quantified into Transcripts Per Kilobase Million (TPM). We removed
1044 cells which had fewer than 800 detected genes or more than 3,000 genes. After filtering, the
1045 mean number of detected genes per cell were 1,765. Then, for the SFB and EAE dataset, we
1046 normalized the gene matrix by SCTransform (Hafemeister and Satija, 2019) regression with
1047 percent of mitochondria reads separately.
1048
1049 **Visualization and clustering**
1050 To visualize the EAE and SFB data, we performed principal component analysis (PCA) for
1051 dimensionality reduction, and further reduced PCA dimensions into two dimensional space using
1052 UMAP (Becht et al., 2018; McInnes and Healy, 2018). UMAP matrix was also used to build the
1053 weighted shared nearest neighbor graph and clustering of single cells was performed by the
1054 original Louvain algorithm. All the above analysis was performed using Seurat v3 R package
1055 (Butler et al., 2018; Stuart et al., 2019). However, we noticed there was one cluster of cells with
1056 a much lower number of features in which over 60% of cells had fewer features than the average.
1057 Thus, it was removed from the analysis.
1058 A table of average gene expression for each cluster, and a table of log2 Fold Change values with
1059 p-values between each sample were calculated with Seurat. Seurat calculates differential
1060 expression based on the non-parameteric Wilcoxon rank sum test. Log fold change is calculated
1061 using the average expression between two groups. These values were used in Figure S1 J. and K.
1062 with IPA for a pathway analysis, and in Figure S1 L. to make volcano plots.
1063

bioRxiv preprint doi: https://doi.org/10.1101/857961; this version posted November 29, 2019. The copyright holder for this preprint (which was not certified by peer review) is the author/funder, who has granted bioRxiv a license to display the preprint in perpetuity. It is made available under aCC-BY-NC 4.0 International license.

Statistical analysis

Differences between groups were calculated using the unpaired two-sided Welch's t-test. Difference between two groups of co-transferred cells, or in bone marrow chimera experiments, were calculated using the paired two-tailed t-test. Differences between EAE clinical score was calculated using two-way ANOVA for repeated measures with Bonferroni correction. For RNA-seq analysis, differential expression was tested by DESeq2 by use of a negative binomial generalized linear model. We treated less than 0.05 of p value as significant differences. $*p < 0.05$, $**p < 0.01$, $***p < 0.001$, and $****p < 0.0001$. Details regarding number of replicates and the definition of center/error bars can be found in figure legends.

DATA AND CODE AVAILABILITY

The bulk RNAseq data and the scRNA seq data supporting the current study have been submitted to GEO, waiting for approval. Once it's approved, we will update the accession number.

Supplemental Information

Supplemental figure legends

Figure S1. Single cell RNAseq analysis of ex vivo CD4$^+$ T cells from spinal cord in the EAE model and the SILP of SFB-colonized mice, related to Figure 1

(A) Experimental design of the scRNAseq analysis. Lethally irradiated *Rag1* KO mice were reconstituted with equal numbers of bone marrow cells from isotype-marked *Il23r*$^{Gfp/+}$ and *Il23r*$^{Gfp/Gfp}$ donors. The CD4$^+$ T cells of both *Il23r* het and KO background in the SC and SILP of each model were sorted for scRNAseq analysis.

bioRxiv preprint doi: https://doi.org/10.1101/857961; this version posted November 29, 2019. The copyright holder for this preprint (which was not certified by peer review) is the author/funder, who has granted bioRxiv a license to display the preprint in perpetuity. It is made available under aCC-BY-NC 4.0 International license.

(B, C) UMAP projections of the scRNAseq data showing the five $CD4^+$ T cell sub-populations in the SILP of SFB colonized mice and the four sub-populations in the SC of EAE mice.

(D, E) Violin plots showing the expression level of selected marker genes for each cluster in the SFB model (D) and the EAE model (E).

(F, G) Distribution of *Il23r*$^{Gfp/+}$ and *Il23r*$^{Gfp/Gfp}$ cells in the UMAP projection of SILP $CD4^+$ T cells (F) and EAE SC $CD4^+$ T cells (G).

(H) Pie chart showing the percentage of *Il23r*^{het} and *Il23r*^{KO} cells in each cluster as in panels D-G. The total number of *Il23r*$^{Gfp/+}$ cells is scaled according to that of *Il23r*$^{Gfp/Gfp}$ cells for the analysis (assuming same number of heterozygous and homozygous cells were analyzed). The actual cell number of each cluster is indicated beneath the corresponding chart.

(I)Validation of marker gene expression in EAE clusters shown in panel E. Top, Klrc1 and Klrd1 are co-expressed on cells that mainly produce IFN-γ (left), but are not expressed on Treg cells (right), and are thus considered as Th1* (IFN-γ producing pathogenic Th17) markers. Bottom left, Treg cells express less Rankl (encoded by *Tnfsf11*). Bottom right, majority of the IFN-γ- and IL-17a-producing cells are $Rankl^+$.

(J, K) Pathway enrichment analysis showing the top 2 pathways activated in EAE-associated Th17 (J) or Th1* (K) cells compared to SFB-induced Th17 cells.

(L, M) Volcano plots based on the scRNAseq analysis showing the differentially expressed genes in EAE-associated Th17 (L) or $Th1^*$ cells (M) compared to SFB-induced Th17 cells. Genes selected for functional screening are highlighted.

Figure S2. Tpi1 is essential for EAE-associated Th17 cell pathogenicity, related to Figure 1

(A) Schematic of the PSIN retroviral vector encoding the Thy1.1 reporter and two gRNAs.

bioRxiv preprint doi: https://doi.org/10.1101/857961; this version posted November 29, 2019. The copyright holder for this preprint (which was not certified by peer review) is the author/funder, who has granted bioRxiv a license to display the preprint in perpetuity. It is made available under aCC-BY-NC 4.0 International license.

(B) Knockout efficiency with single compared to double gRNA vectors. In vitro cultured $CD4^+$ T cells were infected with the retrovirus containing a single or two gRNAs targeting *Cd4,* and Cd4 expression was evaluated 72 h later.

(C) Experimental design for functional screening of pathogenic genes in the transfer EAE model. Naïve 2D2 Cas9 $CD4^+$ T cells were activated in vitro, infected with the double gRNA retrovirus, and differentiated into Th17 cells. Thy1.1 high cells were purified and transferred into *Rag1* KO mice, which were immunized with MOG/CFA at the same time. EAE progression was monitored to evaluate the requirement for each gene in pathogenesis.

(D) Clinical disease course of EAE in *Rag1* KO mice receiving control *(Olfr2* KO) 2D2 cells or candidate gene KO 2D2 cells, and in MOG-CFA-immunized *S100a4* KO and WT littermate control mice (6 pairs). The 2D2 transfer system was validated by failure of 2D2 cells deficient in *Bhlhe40*, a gene known to be essential for T cell pathogenicity, to induce EAE. At least 5 mice were used for each group, and each experiment was repeated at least twice.

(E, F) Sorting strategy for bulk RNAseq analysis of EAE-associated Th17, $Th1^*$, Treg (E) and SFB-induced Th17 and Treg cells (F).

Figure S3. *Tpi1* is essential for the differentiation of all $CD4^+$ T cells, related to Figure 1

(A, B) Impaired RORγt, Foxp3, IL-17a and IFN-γ expression by *Tpi1* mutant compared to WT $CD4^+$ T cells in the mLN (A) and the SILP (B) of reconstituted mixed bone marrow chimeric mice colonized with SFB. Left panels, representative FACS plots showing RORγt/Foxp3 and IL-17a/IFN-γ expression in paired *Tpi1* WT (red) and KO (blue) $CD4^+$ T cells in each mouse.

bioRxiv preprint doi: https://doi.org/10.1101/857961; this version posted November 29, 2019. The copyright holder for this preprint (which was not certified by peer review) is the author/funder, who has granted bioRxiv a license to display the preprint in perpetuity. It is made available under aCC-BY-NC 4.0 International license.

Middle panels, frequencies of each $CD4^+$ T cell subtype among the *Tpi1* WT and *Tpi1* KO cells. Right panels, *Tpi1* KO/*Tpi1* WT ratios for each $CD4^+$ T cell subtype in mLN and SILP.

(C) Impaired RORγt, Foxp3, IL-17a and IFN-γ expression in *Tpi1* mutant compared to WT $CD4^+$ T cells in the dLN of mixed bone marrow reconstituted mice, at day 15 of MOG-induced EAE. The number of *Tpi1* KO $CD4^+$ T cells obtained from SC was too low for a meaningful subtype analysis, and hence is not shown. Panels are organized as in (B).

Figure S4. Electroporation-based CRISPR-mediated targeting of metabolic genes in naïve $CD4^+$ T cells, related to Figure 2

(A) Map of metabolic pathways, showing relevant genes and metabolites in glycolysis, PPP and the TCA cycle. The biosynthetic processes from glycolysis metabolites are labeled in green. Genes that were targeted using CRISPR in this study are labeled in blue. Gpi1, Tpi1 and Ldha are the three enzymes that are expected to not be essential for glycolysis: (1) The reaction catalyzed by Gpi1 (glucose-6-phosphate to fructose-1,6-bisphosphate) can also be achieved by the PPP, making Gpi1 possibly redundant for this reaction; (2) Tpi1 controls the inter conversion of glyceraldehyde-3-phosphate and dihydroxyacetone phosphate, the two 3-carbon molecules generated by degrading fructose-1,6-phosphate. Loss of Tpi1 should lead to the loss of 50%, but not all of the glycolytic activity, and thus may be not lethal; (3) Ldha controls the conversion of pyruvate to lactic acid, and the regeneration of NAD^+. However, pyruvate could still enter the TCA cycle in Ldha-deficient cells, for energy production and biomass synthesis.

(B) Schematic of gene targeting in naïve T cells. Left, PCR amplicons encoding gRNAs were electroporated into Cas9-expressing naïve $CD4^+$ T cells, which were subsequently cultured in

bioRxiv preprint doi: https://doi.org/10.1101/857961; this version posted November 29, 2019. The copyright holder for this preprint (which was not certified by peer review) is the author/funder, who has granted bioRxiv a license to display the preprint in perpetuity. It is made available under aCC-BY-NC 4.0 International license.

vitro or transferred into recipient mice. Right, *in vivo* KO efficiency can be assessed by measuring the KO efficiency of the in vitro cultured Th17 cells. Cas9-expressing 7B8 naïve $CD4^+$ T cells were electroporated with *Gfp* guide amplicons to target the Gfp that is co-expressed with Cas9 at the Rosa26 locus, and then cultured *in vitro* in Th17 conditions (IL6+TGF-β), or transferred into SFB-colonized mice. Gfp expression was examined 4 days later in the in vitro cultured Th17 cells (top) and the ex vivo cells isolated from the mLN (bottom).

(C-E) Evaluation of the knockout efficiency of guides used in this study with in vitro Th17 cell culture. 8000 electroporated naïve $CD4^+$ T cells were seeded in each well at the beginning of Th17 cell culture. Because gene function is related to cell growth and differentiation, we estimated the KO efficiency based on three variable factors at 120 h post electroporation: protein expression level (C), live cell number (D), and IL-17a production (E). Taking *Gapdh* targeting as an example, western blot data shows Gapdh protein expression decreased only ~40%. However, the cell number was reduced ~70%, and IL-17a production by live cells was further reduced more than 50% compared to the *Olfr2* control. Taken together, we estimate that the Gapdh guide achieved more than 80% knockout *in vitro*. Data are representative of three independent experiments.

(F) Efficiency of gene inactivation following electroporation of naïve Cas9 $CD4^+$ T cells with a mixture of two guide amplicons targeting *Cd4* and *Cd45* in cultured Th17 cells at 96 h.

P values were determined using t tests.

Figure S5. Differentiation of glycolysis gene-targeted 7B8 T cells in the SILP of SFB-colonized mice, related to Figure 2

bioRxiv preprint doi: https://doi.org/10.1101/857961; this version posted November 29, 2019. The copyright holder for this preprint (which was not certified by peer review) is the author/funder, who has granted bioRxiv a license to display the preprint in perpetuity. It is made available under aCC-BY-NC 4.0 International license.

(A) Representative FACS plots showing the expression of RORγt and Foxp3 in the *Olfr2* KO control cells and the co-transferred *Olfr2* control or glycolysis gene KO cells in the SILP at day 15 post transfer.

(B) Left, summary of the Th17 frequencies (RORγt$^+$ Foxp3$^-$) in the *Olfr2* KO control cells (green) and the co-transferred *Olfr2* control or glycolysis gene KO cells (red), as in panel (A). Right, the KO/Olfr2 ratios of Th17 frequencies.

(C) Representative FACS plots showing IL-17a expression in *Olfr2* control and co-transferred *Olfr2* control or glycolysis gene KO Th17 cells (RORγt$^+$ Foxp3$^-$ cells) isolated from the SILP at day 15 post transfer and following *in vitro* PMA/Ionomycin re-stimulation.

(D) Left, summary of IL-17a expression based on results in panel (C). Right, KO/*Olfr2* ratios of IL-17a expression.

P values were determined using t tests.

Figure S6. Hypoxic microenvironment in the EAE spinal cord impairs proliferation of *Gpi1*-deficient Th17 cells, related to Figure 6

(A, B) The PPP contributes to Th17 cell accumulation in the SC in EAE. (A) Representative FACS plots showing the frequencies of co-transferred *Olfr2* KO and *Olfr2* control or *G6pdx* KO 2D2 T cells in the EAE SC at day 15. (B) Compilation of KO/*Olfr2* cell number ratios as shown in panel A.

(C, D) Pimonidazole staining of different CD4$^+$ T cell subsets in the SFB and EAE models. (C) Representative FACS plots showing pimonidazole staining of each subtype of CD4$^+$ T cell in the mLN and the SILP of SFB-colonized healthy mice and in the dLN and the SC of EAE

bioRxiv preprint doi: https://doi.org/10.1101/857961; this version posted November 29, 2019. The copyright holder for this preprint (which was not certified by peer review) is the author/funder, who has granted bioRxiv a license to display the preprint in perpetuity. It is made available under aCC-BY-NC 4.0 International license.

mice. Treg (Foxp3$^+$ RORγt$^-$ Tbet$^-$), Th17 (RORγt$^+$ Foxp3$^-$Tbet$^-$), Th1 (Tbet$^+$ RORγt$^-$ Foxp3$^-$), Triple$^-$ (RORγt$^-$ Tbet$^-$ Foxp3$^-$). (D) Summarized pimonidazole staining based on panel C.

(E) Transcription factor staining in CD4$^+$ T cells from *Hif1a* WT and KO mice colonized with SFB (top, cells from SILP)) or subjected to EAE (bottom, from SC at day15). Left, representative FACS plots showing the frequencies of Th17 cells (RORγt$^+$ Foxp3$^-$) and Treg cells (Foxp3$^+$ RORγt$^-$) among total *Hif1a* WT and KO CD4$^+$ T cells; Right, summary of transcription factor staining from two independent experiments.

(F) Cytokine production in CD4$^+$ T cells from *Hif1a* WT and KO CD4 T cells in the SFB (top) and EAE (bottom) models after in vitro PMA/ionomycin restimulation. Left, representative plots showing the frequencies of IL-17a producing cells among RORγt$^+$ Foxp3$^-$ *Hif1a* WT or KO cells in the SILP of SFB-colonized mice (top) and frequencies of IL-17a, IL-17a/IFN-γ, and IFN-γ producing cells among Foxp3$^-$ *Hif1a* WT or KO cells in the SC at day 15 after EAE induction (bottom); Right, summary of cytokine production from two independent experiments. .

(G) Left, representative plots showing EDU incorporation in co-transferred *Olfr2* and *Olfr2* control or *Gpi1* KO 2D2 cells at different days post transfer in the dLNs. Right, compiled data of one representative experiment. Two independent experiments were performed with the same conclusion.

(H, I) Proliferation of dLN 2D2 cells in the EAE model and mLN 7B8 cells in SFB-colonized mice. Naïve 7B8 or 2D2 CD4$^+$ T cells were labeled with CFSE and 100K cells were transferred into recipient mice that had been previously colonized with SFB or were immunized with MOG/CFA immediately after cell transfer. The mLN of the 7B8 model and dLN of the EAE model were collected at different time points for cell division analysis. (H)

bioRxiv preprint doi: https://doi.org/10.1101/857961; this version posted November 29, 2019. The copyright holder for this preprint (which was not certified by peer review) is the author/funder, who has granted bioRxiv a license to display the preprint in perpetuity. It is made available under aCC-BY-NC 4.0 International license.

Left, representative FACS plot showing CFSE labeling of the 7B8 and 2D2 cells at different time points. Right, pie charts showing the frequencies of cells with different numbers of divisions. Division number was labeled in different colors. (I) Total cell number count of mLN 7B8 cells and dLN 2D2 cells at different time points. For each time point, 4-10 mice were used for each group. Two independent experiments were performed with the same conclusion.

(J, K) Left, compiled data showing the frequencies of $Ccr6^+$ cells among co-transferred *Olfr2* and *Olfr2* control or *Gpi1* KO 2D2 cells in the dLN at day 9 (J) or in the SC at day 13 (K) post transfer and EAE induction. Right, the KO/WT ratios of the $Ccr6^+$ frequencies. Two independent experiments were performed with same conclusion.

(L) Compiled data showing the frequencies of active $Caspase3^+$ cells among co-transferred *Olfr2* and *Olfr2* control or *Gpi1* KO 2D2 cells in the SC at day 10 post transfer and EAE induction. n=10.

P values of panel B, I, J and K were determined using t tests. P values of panel E, F, and L were determined using

References

bioRxiv preprint doi: https://doi.org/10.1101/857961; this version posted November 29, 2019. The copyright holder for this preprint (which was not certified by peer review) is the author/funder, who has granted bioRxiv a license to display the preprint in perpetuity. It is made available under aCC-BY-NC 4.0 International license.

1246 Ahern, P.P., Schiering, C., Buonocore, S., McGeachy, M.J., Cua, D.J., Maloy, K.J., and Powrie, F.
1247 (2010). Interleukin-23 Drives Intestinal Inflammation through Direct Activity on T Cells.
1248 Immunity *33*, 279-288.
1249 Awasthi, A., Riol-Blanco, L., Jager, A., Korn, T., Pot, C., Galileos, G., Bettelli, E., Kuchroo, V.K., and
1250 Oukka, M. (2009). Cutting edge: IL-23 receptor gfp reporter mice reveal distinct
1251 populations of IL-17-producing cells. J Immunol *182*, 5904-5908.
1252 Baronciani, L., Zanella, A., Bianchi, P., Zappa, M., Alfinito, F., Iolascon, A., Tannoia, N., Beutler,
1253 E., and Sirchia, G. (1996). Study of the molecular defects in glucose phosphate isomerase-
1254 deficient patients affected by chronic hemolytic anemia. Blood *88*, 2306-2310.
1255 Becht, E., McInnes, L., Healy, J., Dutertre, C.A., Kwok, I.W.H., Ng, L.G., Ginhoux, F., and Newell,
1256 E.W. (2018). Dimensionality reduction for visualizing single-cell data using UMAP. Nat
1257 Biotechnol.
1258 Berod, L., Friedrich, C., Nandan, A., Freitag, J., Hagemann, S., Harmrolfs, K., Sandouk, A., Hesse,
1259 C., Castro, C.N., Bahre, H.*, et al.* (2014). De novo fatty acid synthesis controls the fate
1260 between regulatory T and T helper 17 cells. Nat Med *20*, 1327-1333.
1261 Bettelli, E., Pagany, M., Weiner, H.L., Linington, C., Sobel, R.A., and Kuchroo, V.K. (2003). Myelin
1262 oligodendrocyte glycoprotein-specific T cell receptor transgenic mice develop spontaneous
1263 autoimmune optic neuritis. J Exp Med *197*, 1073-1081.
1264 Bhattarai, D., Xu, X., and Lee, K. (2018). Hypoxia-inducible factor-1 (HIF-1) inhibitors from the
1265 last decade (2007 to 2016): A "structure-activity relationship" perspective. Med Res Rev *38*,
1266 1404-1442.

bioRxiv preprint doi: https://doi.org/10.1101/857961; this version posted November 29, 2019. The copyright holder for this preprint (which was not certified by peer review) is the author/funder, who has granted bioRxiv a license to display the preprint in perpetuity. It is made available under aCC-BY-NC 4.0 International license.

1267 Birsoy, K., Wang, T., Chen, W.W., Freinkman, E., Abu-Remaileh, M., and Sabatini, D.M. (2015).
1268 An Essential Role of the Mitochondrial Electron Transport Chain in Cell Proliferation Is to
1269 Enable Aspartate Synthesis. Cell *162*, 540-551.
1270 Bray, N.L., Pimentel, H., Melsted, P., and Pachter, L. (2016). Near-optimal probabilistic RNA-seq
1271 quantification. Nat Biotechnol *34*, 525-527.
1272 Bulcha, J.T., Giese, G.E., Ali, M.Z., Lee, Y.U., Walker, M.D., Holdorf, A.D., Yilmaz, L.S., Brewster,
1273 R.C., and Walhout, A.J.M. (2019). A Persistence Detector for Metabolic Network Rewiring
1274 in an Animal. Cell Rep *26*, 460-468 e464.
1275 Butler, A., Hoffman, P., Smibert, P., Papalexi, E., and Satija, R. (2018). Integrating single-cell
1276 transcriptomic data across different conditions, technologies, and species. Nat Biotechnol
1277 *36*, 411-420.
1278 Cua, D.J., Sherlock, J., Chen, Y., Murphy, C.A., Joyce, B., Seymour, B., Lucian, L., To, W., Kwan, S.,
1279 Churakova, T.*, et al.* (2003). Interleukin-23 rather than interleukin-12 is the critical cytokine
1280 for autoimmune inflammation of the brain. Nature *421*, 744-748.
1281 Dang, E.V., Barbi, J., Yang, H.Y., Jinasena, D., Yu, H., Zheng, Y., Bordman, Z., Fu, J., Kim, Y., Yen,
1282 H.R.*, et al.* (2011). Control of T(H)17/T(reg) balance by hypoxia-inducible factor 1. Cell *146*,
1283 772-784.
1284 Davies, A.L., Desai, R.A., Bloomfield, P.S., McIntosh, P.R., Chapple, K.J., Linington, C., Fairless, R.,
1285 Diem, R., Kasti, M., Murphy, M.P.*, et al.* (2013). Neurological deficits caused by tissue
1286 hypoxia in neuroinflammatory disease. Ann Neurol *74*, 815-825.
1287 de Padua, M.C., Delodi, G., Vucetic, M., Durivault, J., Vial, V., Bayer, P., Noleto, G.R., Mazure,
1288 N.M., Zdralevic, M., and Pouyssegur, J. (2017). Disrupting glucose-6-phosphate isomerase

bioRxiv preprint doi: https://doi.org/10.1101/857961; this version posted November 29, 2019. The copyright holder for this preprint (which was not certified by peer review) is the author/funder, who has granted bioRxiv a license to display the preprint in perpetuity. It is made available under aCC-BY-NC 4.0 International license.

1289 fully suppresses the "Warburg effect" and activates OXPHOS with minimal impact on tumor
1290 growth except in hypoxia. Oncotarget *8*, 87623-87637.
1291 Delgoffe, G.M., Kole, T.P., Zheng, Y., Zarek, P.E., Matthews, K.L., Xiao, B., Worley, P.F., Kozma,
1292 S.C., and Powell, J.D. (2009). The mTOR kinase differentially regulates effector and
1293 regulatory T cell lineage commitment. Immunity *30*, 832-844.
1294 Deutscher, D., Meilijson, I., Kupiec, M., and Ruppin, E. (2006). Multiple knockout analysis of
1295 genetic robustness in the yeast metabolic network. Nat Genet *38*, 993-998.
1296 Fernandez, C.A., DesRosiers, C., Previs, S.F., David, F., and Brunengraber, H. (1996). Correction
1297 of C-13 mass isotopomer distributions for natural stable isotope abundance. J Mass
1298 Spectrom *31*, 255-262.
1299 Fox, C.J., Hammerman, P.S., and Thompson, C.B. (2005). Fuel feeds function: energy
1300 metabolism and the T-cell response. Nat Rev Immunol *5*, 844-852.
1301 Gerriets, V.A., and Rathmell, J.C. (2012). Metabolic pathways in T cell fate and function. Trends
1302 Immunol *33*, 168-173.
1303 Ghoreschi, K., Laurence, A., Yang, X.P., Tato, C.M., McGeachy, M.J., Konkel, J.E., Ramos, H.L.,
1304 Wei, L., Davidson, T.S., Bouladoux, N.*, et al.* (2010). Generation of pathogenic T(H)17 cells
1305 in the absence of TGF-beta signalling. Nature *467*, 967-971.
1306 Grassian, A.R., Parker, S.J., Davidson, S.M., Divakaruni, A.S., Green, C.R., Zhang, X., Slocum, K.L.,
1307 Pu, M., Lin, F., Vickers, C.*, et al.* (2014). IDH1 mutations alter citric acid cycle metabolism
1308 and increase dependence on oxidative mitochondrial metabolism. Cancer Res *74*, 3317-
1309 3331.

bioRxiv preprint doi: https://doi.org/10.1101/857961; this version posted November 29, 2019. The copyright holder for this preprint (which was not certified by peer review) is the author/funder, who has granted bioRxiv a license to display the preprint in perpetuity. It is made available under aCC-BY-NC 4.0 International license.

1310 Hafemeister, C., and Satija, R. (2019). Normalization and variance stabilization of single-cell
1311 RNA-seq data using regularized negative binomial regression. bioRxiv, 576827.
1312 Hirota, K., Duarte, J.H., Veldhoen, M., Hornsby, E., Li, Y., Cua, D.J., Ahlfors, H., Wilhelm, C.,
1313 Tolaini, M., Menzel, U*., et al.* (2011). Fate mapping of IL-17-producing T cells in
1314 inflammatory responses. Nat Immunol *12*, 255-263.
1315 Hirota, K., Hashimoto, M., Yoshitomi, H., Tanaka, S., Nomura, T., Yamaguchi, T., Iwakura, Y.,
1316 Sakaguchi, N., and Sakaguchi, S. (2007). T cell self-reactivity forms a cytokine milieu for
1317 spontaneous development of IL-17(+) Th cells that cause autoimmune arthritis. Journal of
1318 Experimental Medicine *204*, 41-47.
1319 Horlbeck, M.A., Xu, A., Wang, M., Bennett, N.K., Park, C.Y., Bogdanoff, D., Adamson, B., Chow,
1320 E.D., Kampmann, M., Peterson, T.R*., et al.* (2018). Mapping the Genetic Landscape of
1321 Human Cells. Cell *174*, 953-967 e922.
1322 Hue, S., Ahern, P., Buonocore, S., Kullberg, M.C., Cua, D.J., McKenzie, B.S., Powrie, F., and
1323 Maloy, K.J. (2006). Interleukin-23 drives innate and T cell-mediated intestinal
1324 inflammation. J Exp Med *203*, 2473-2483.
1325 Ivanov, II, Atarashi, K., Manel, N., Brodie, E.L., Shima, T., Karaoz, U., Wei, D., Goldfarb, K.C.,
1326 Santee, C.A., Lynch, S.V*., et al.* (2009). Induction of intestinal Th17 cells by segmented
1327 filamentous bacteria. Cell *139*, 485-498.
1328 Ivanov, II, McKenzie, B.S., Zhou, L., Tadokoro, C.E., Lepelley, A., Lafaille, J.J., Cua, D.J., and
1329 Littman, D.R. (2006). The orphan nuclear receptor RORgammat directs the differentiation
1330 program of proinflammatory IL-17+ T helper cells. Cell *126*, 1121-1133.

bioRxiv preprint doi: https://doi.org/10.1101/857961; this version posted November 29, 2019. The copyright holder for this preprint (which was not certified by peer review) is the author/funder, who has granted bioRxiv a license to display the preprint in perpetuity. It is made available under aCC-BY-NC 4.0 International license.

1331 Johnson, M.O., Wolf, M.M., Madden, M.Z., Andrejeva, G., Sugiura, A., Contreras, D.C., Maseda,
1332 D., Liberti, M.V., Paz, K., Kishton, R.J*., et al.* (2018). Distinct Regulation of Th17 and Th1 Cell
1333 Differentiation by Glutaminase-Dependent Metabolism. Cell *175*, 1780-1795 e1719.
1334 Johnson, T.W., Wu, Y., Nathoo, N., Rogers, J.A., Wee Yong, V., and Dunn, J.F. (2016). Gray
1335 Matter Hypoxia in the Brain of the Experimental Autoimmune Encephalomyelitis Model of
1336 Multiple Sclerosis. PLoS One *11*, e0167196.
1337 Kanno, H., Fujii, H., Hirono, A., Ishida, Y., Ohga, S., Fukumoto, Y., Matsuzawa, K., Ogawa, S., and
1338 Miwa, S. (1996). Molecular analysis of glucose phosphate isomerase deficiency associated
1339 with hereditary hemolytic anemia. Blood *88*, 2321-2325.
1340 Karhausen, J., Furuta, G.T., Tomaszewski, J.E., Johnson, R.S., Colgan, S.P., and Haase, V.H.
1341 (2004). Epithelial hypoxia-inducible factor-1 is protective in murine experimental colitis. J
1342 Clin Invest *114*, 1098-1106.
1343 Kugler, W., Breme, K., Laspe, P., Muirhead, H., Davies, C., Winkler, H., Schroter, W., and
1344 Lakomek, M. (1998). Molecular basis of neurological dysfunction coupled with haemolytic
1345 anaemia in human glucose-6-phosphate isomerase (GPI) deficiency. Hum Genet *103*, 450-
1346 454.
1347 Kullberg, M.C., Jankovic, D., Feng, C.G., Hue, S., Gorelick, P.L., McKenzie, B.S., Cua, D.J., Powrie,
1348 F., Cheever, A.W., Maloy, K.J*., et al.* (2006). IL-23 plays a key role in Helicobacter hepaticus-
1349 induced T cell-dependent colitis. J Exp Med *203*, 2485-2494.
1350 Kumar, P., Monin, L., Castillo, P., Elsegeiny, W., Horne, W., Eddens, T., Vikram, A., Good, M.,
1351 Schoenborn, A.A., Bibby, K*., et al.* (2016). Intestinal Interleukin-17 Receptor Signaling

bioRxiv preprint doi: https://doi.org/10.1101/857961; this version posted November 29, 2019. The copyright holder for this preprint (which was not certified by peer review) is the author/funder, who has granted bioRxiv a license to display the preprint in perpetuity. It is made available under aCC-BY-NC 4.0 International license.

Mediates Reciprocal Control of the Gut Microbiota and Autoimmune Inflammation. Immunity *44*, 659-671.

Lee, W.N., Boros, L.G., Puigjaner, J., Bassilian, S., Lim, S., and Cascante, M. (1998). Mass isotopomer study of the nonoxidative pathways of the pentose cycle with [1,2-13C2]glucose. Am J Physiol *274*, E843-851.

Lewis, C.A., Parker, S.J., Fiske, B.P., McCloskey, D., Gui, D.Y., Green, C.R., Vokes, N.I., Feist, A.M., Vander Heiden, M.G., and Metallo, C.M. (2014). Tracing compartmentalized NADPH metabolism in the cytosol and mitochondria of mammalian cells. Mol Cell *55*, 253-263.

Li, Z.H., Dulyaninova, N.G., House, R.P., Almo, S.C., and Bresnick, A.R. (2010). S100A4 regulates macrophage chemotaxis. Mol Biol Cell *21*, 2598-2610.

Liberti, M.V., Dai, Z.W., Wardell, S.E., Baccile, J.A., Liu, X.J., Gao, X., Baldi, R., Mehrmohamadi, M., Johnson, M.O., Madhukar, N.S*., et al.* (2017). A Predictive Model for Selective Targeting of the Warburg Effect through GAPDH Inhibition with a Natural Product. Cell Metab *26*, 648-+.

MacIver, N.J., Michalek, R.D., and Rathmell, J.C. (2013). Metabolic regulation of T lymphocytes. Annu Rev Immunol *31*, 259-283.

Mao, K., Baptista, A.P., Tamoutounour, S., Zhuang, L., Bouladoux, N., Martins, A.J., Huang, Y., Gerner, M.Y., Belkaid, Y., and Germain, R.N. (2018). Innate and adaptive lymphocytes sequentially shape the gut microbiota and lipid metabolism. Nature *554*, 255-259.

McGeachy, M.J., Chen, Y., Tato, C.M., Laurence, A., Joyce-Shaikh, B., Blumenschein, W.M., McClanahan, T.K., O'Shea, J.J., and Cua, D.J. (2009). The interleukin 23 receptor is essential

bioRxiv preprint doi: https://doi.org/10.1101/857961; this version posted November 29, 2019. The copyright holder for this preprint (which was not certified by peer review) is the author/funder, who has granted bioRxiv a license to display the preprint in perpetuity. It is made available under aCC-BY-NC 4.0 International license.

for the terminal differentiation of interleukin 17-producing effector T helper cells in vivo. Nat Immunol *10*, 314-324.

McInnes, L., and Healy, J. (2018). UMAP: Uniform Manifold Approximation and Projection for Dimension Reduction. ArXiv *abs/1802.03426*.

McMullin, M.F. (1999). The molecular basis of disorders of red cell enzymes. J Clin Pathol *52*, 241-244.

Metallo, C.M., Gameiro, P.A., Bell, E.L., Mattaini, K.R., Yang, J., Hiller, K., Jewell, C.M., Johnson, Z.R., Irvine, D.J., Guarente, L*., et al.* (2011). Reductive glutamine metabolism by IDH1 mediates lipogenesis under hypoxia. Nature *481*, 380-384.

Michalek, R.D., Gerriets, V.A., Jacobs, S.R., Macintyre, A.N., MacIver, N.J., Mason, E.F., Sullivan, S.A., Nichols, A.G., and Rathmell, J.C. (2011). Cutting edge: distinct glycolytic and lipid oxidative metabolic programs are essential for effector and regulatory CD4+ T cell subsets. J Immunol *186*, 3299-3303.

Milner, J.D., and Holland, S.M. (2013). The cup runneth over: lessons from the ever-expanding pool of primary immunodeficiency diseases. Nat Rev Immunol *13*, 635-648.

Morrison, P.J., Bending, D., Fouser, L.A., Wright, J.F., Stockinger, B., Cooke, A., and Kullberg, M.C. (2013). Th17-cell plasticity in Helicobacter hepaticus-induced intestinal inflammation. Mucosal Immunol *6*, 1143-1156.

Murphy, C.A., Langrish, C.L., Chen, Y., Blumenschein, W., McClanahan, T., Kastelein, R.A., Sedgwick, J.D., and Cua, D.J. (2003). Divergent pro- and antiinflammatory roles for IL-23 and IL-12 in joint autoimmune inflammation. J Exp Med *198*, 1951-1957.

bioRxiv preprint doi: https://doi.org/10.1101/857961; this version posted November 29, 2019. The copyright holder for this preprint (which was not certified by peer review) is the author/funder, who has granted bioRxiv a license to display the preprint in perpetuity. It is made available under aCC-BY-NC 4.0 International license.

1394 Nakae, S., Nambu, A., Sudo, K., and Iwakura, Y. (2003a). Suppression of immune induction of
1395 collagen-induced arthritis in IL-17-deficient mice. J Immunol *171*, 6173-6177.
1396 Nakae, S., Saijo, S., Horai, R., Sudo, K., Mori, S., and Iwakura, Y. (2003b). IL-17 production from
1397 activated T cells is required for the spontaneous development of destructive arthritis in
1398 mice deficient in IL-1 receptor antagonist. P Natl Acad Sci USA *100*, 5986-5990.
1399 Naughton, D.P., Haywood, R., Blake, D.R., Edmonds, S., Hawkes, G.E., and Grootveld, M. (1993).
1400 A comparative evaluation of the metabolic profiles of normal and inflammatory knee-joint
1401 synovial fluids by high resolution proton NMR spectroscopy. FEBS Lett *332*, 221-225.
1402 Ng, C., Aichinger, M., Nguyen, T., Au, C., Najar, T., Wu, L., Mesa, K.R., Liao, W., Quivy, J.P.,
1403 Hubert, B.*, et al.* (2019). The histone chaperone CAF-1 cooperates with the DNA
1404 methyltransferases to maintain Cd4 silencing in cytotoxic T cells. Genes Dev *33*, 669-683.
1405 Ng, C.T., Biniecka, M., Kennedy, A., McCormick, J., Fitzgerald, O., Bresnihan, B., Buggy, D.,
1406 Taylor, C.T., O'Sullivan, J., Fearon, U.*, et al.* (2010). Synovial tissue hypoxia and
1407 inflammation in vivo. Ann Rheum Dis *69*, 1389-1395.
1408 O'Quinn, D.B., Palmer, M.T., Lee, Y.K., and Weaver, C.T. (2008). Emergence of the Th17 pathway
1409 and its role in host defense. Adv Immunol *99*, 115-163.
1410 Okada, S., Markle, J.G., Deenick, E.K., Mele, F., Averbuch, D., Lagos, M., Alzahrani, M., Al-
1411 Muhsen, S., Halwani, R., Ma, C.S.*, et al.* (2015). IMMUNODEFICIENCIES. Impairment of
1412 immunity to Candida and Mycobacterium in humans with bi-allelic RORC mutations.
1413 Science *349*, 606-613.

bioRxiv preprint doi: https://doi.org/10.1101/857961; this version posted November 29, 2019. The copyright holder for this preprint (which was not certified by peer review) is the author/funder, who has granted bioRxiv a license to display the preprint in perpetuity. It is made available under aCC-BY-NC 4.0 International license.

1414 Omenetti, S., Bussi, C., Metidji, A., Iseppon, A., Lee, S., Tolaini, M., Li, Y., Kelly, G., Chakravarty,
1415 P., Shoaie, S*., et al.* (2019). The Intestine Harbors Functionally Distinct Homeostatic Tissue-
1416 Resident and Inflammatory Th17 Cells. Immunity *51*, 77-89 e76.
1417 Pacold, M.E., Brimacombe, K.R., Chan, S.H., Rohde, J.M., Lewis, C.A., Swier, L.J., Possemato, R.,
1418 Chen, W.W., Sullivan, L.B., Fiske, B.P*., et al.* (2016). A PHGDH inhibitor reveals coordination
1419 of serine synthesis and one-carbon unit fate. Nat Chem Biol *12*, 452-458.
1420 Palmer, C.S., Ostrowski, M., Balderson, B., Christian, N., and Crowe, S.M. (2015). Glucose
1421 metabolism regulates T cell activation, differentiation, and functions. Front Immunol *6*, 1.
1422 Patel, C.H., and Powell, J.D. (2017). Targeting T cell metabolism to regulate T cell activation,
1423 differentiation and function in disease. Curr Opin Immunol *46*, 82-88.
1424 Peters, C.L., Morris, C.J., Mapp, P.I., Blake, D.R., Lewis, C.E., and Winrow, V.R. (2004). The
1425 transcription factors hypoxia-inducible factor 1alpha and Ets-1 colocalize in the hypoxic
1426 synovium of inflamed joints in adjuvant-induced arthritis. Arthritis Rheum *50*, 291-296.
1427 Picelli, S., Faridani, O.R., Bjorklund, A.K., Winberg, G., Sagasser, S., and Sandberg, R. (2014). Full-
1428 length RNA-seq from single cells using Smart-seq2. Nat Protoc *9*, 171-181.
1429 Piskin, G., Sylva-Steenland, R.M., Bos, J.D., and Teunissen, M.B. (2006). In vitro and in situ
1430 expression of IL-23 by keratinocytes in healthy skin and psoriasis lesions: enhanced
1431 expression in psoriatic skin. J Immunol *176*, 1908-1915.
1432 Platt, R.J., Chen, S., Zhou, Y., Yim, M.J., Swiech, L., Kempton, H.R., Dahlman, J.E., Parnas, O.,
1433 Eisenhaure, T.M., Jovanovic, M*., et al.* (2014). CRISPR-Cas9 knockin mice for genome
1434 editing and cancer modeling. Cell *159*, 440-455.

bioRxiv preprint doi: https://doi.org/10.1101/857961; this version posted November 29, 2019. The copyright holder for this preprint (which was not certified by peer review) is the author/funder, who has granted bioRxiv a license to display the preprint in perpetuity. It is made available under aCC-BY-NC 4.0 International license.

1435 Powell, J.D., Pollizzi, K.N., Heikamp, E.B., and Horton, M.R. (2012). Regulation of immune
1436 responses by mTOR. Annu Rev Immunol *30*, 39-68.
1437 Puel, A., Cypowyj, S., Bustamante, J., Wright, J.F., Liu, L., Lim, H.K., Migaud, M., Israel, L.,
1438 Chrabieh, M., Audry, M.*, et al.* (2011). Chronic mucocutaneous candidiasis in humans with
1439 inborn errors of interleukin-17 immunity. Science *332*, 65-68.
1440 Raez, L.E., Papadopoulos, K., Ricart, A.D., Chiorean, E.G., Dipaola, R.S., Stein, M.N., Rocha Lima,
1441 C.M., Schlesselman, J.J., Tolba, K., Langmuir, V.K.*, et al.* (2013). A phase I dose-escalation
1442 trial of 2-deoxy-D-glucose alone or combined with docetaxel in patients with advanced
1443 solid tumors. Cancer Chemother Pharmacol *71*, 523-530.
1444 Schneider, A.S. (2000). Triosephosphate isomerase deficiency: historical perspectives and
1445 molecular aspects. Best Pract Res Cl Ha *13*, 119-140.
1446 Segre, D., Deluna, A., Church, G.M., and Kishony, R. (2005). Modular epistasis in yeast
1447 metabolism. Nat Genet *37*, 77-83.
1448 Semenza, G.L. (2003). Targeting HIF-1 for cancer therapy. Nat Rev Cancer *3*, 721-732.
1449 Semenza, G.L. (2014). Oxygen sensing, hypoxia-inducible factors, and disease pathophysiology.
1450 Annu Rev Pathol *9*, 47-71.
1451 Shi, L.Z., Wang, R., Huang, G., Vogel, P., Neale, G., Green, D.R., and Chi, H. (2011). HIF1alpha-
1452 dependent glycolytic pathway orchestrates a metabolic checkpoint for the differentiation
1453 of TH17 and Treg cells. J Exp Med *208*, 1367-1376.
1454 Stuart, T., Butler, A., Hoffman, P., Hafemeister, C., Papalexi, E., Mauck, W.M., 3rd, Hao, Y.,
1455 Stoeckius, M., Smibert, P., and Satija, R. (2019). Comprehensive Integration of Single-Cell
1456 Data. Cell *177*, 1888-1902 e1821.

bioRxiv preprint doi: https://doi.org/10.1101/857961; this version posted November 29, 2019. The copyright holder for this preprint (which was not certified by peer review) is the author/funder, who has granted bioRxiv a license to display the preprint in perpetuity. It is made available under aCC-BY-NC 4.0 International license.

1457 Sullivan, L.B., Gui, D.Y., Hosios, A.M., Bush, L.N., Freinkman, E., and Vander Heiden, M.G. (2015).
1458 Supporting Aspartate Biosynthesis Is an Essential Function of Respiration in Proliferating
1459 Cells. Cell *162*, 552-563.
1460 Thiele, I., Vo, T.D., Price, N.D., and Palsson, B.O. (2005). Expanded metabolic reconstruction of
1461 Helicobacter pylori (iIT341 GSM/GPR): an in silico genome-scale characterization of single-
1462 and double-deletion mutants. J Bacteriol *187*, 5818-5830.
1463 Van Welden, S., Selfridge, A.C., and Hindryckx, P. (2017). Intestinal hypoxia and hypoxia-
1464 induced signalling as therapeutic targets for IBD. Nat Rev Gastroenterol Hepatol *14*, 596-
1465 611.
1466 Vander Heiden, M.G., Cantley, L.C., and Thompson, C.B. (2009). Understanding the Warburg
1467 effect: the metabolic requirements of cell proliferation. Science *324*, 1029-1033.
1468 Veldhoen, M., Hocking, R.J., Atkins, C.J., Locksley, R.M., and Stockinger, B. (2006). TGFbeta in
1469 the context of an inflammatory cytokine milieu supports de novo differentiation of IL-17-
1470 producing T cells. Immunity *24*, 179-189.
1471 Warburg, O., Gawehn, K., and Geissler, A.W. (1958). [Metabolism of leukocytes]. Z Naturforsch
1472 B *13B*, 515-516.
1473 Xu, M., Pokrovskii, M., Ding, Y., Yi, R., Au, C., Harrison, O.J., Galan, C., Belkaid, Y., Bonneau, R.,
1474 and Littman, D.R. (2018). c-MAF-dependent regulatory T cells mediate immunological
1475 tolerance to a gut pathobiont. Nature *554*, 373-377.
1476 Yang, R., and Dunn, J.F. (2015). Reduced cortical microvascular oxygenation in multiple
1477 sclerosis: a blinded, case-controlled study using a novel quantitative near-infrared
1478 spectroscopy method. Sci Rep *5*, 16477.

bioRxiv preprint doi: https://doi.org/10.1101/857961; this version posted November 29, 2019. The copyright holder for this preprint (which was not certified by peer review) is the author/funder, who has granted bioRxiv a license to display the preprint in perpetuity. It is made available under aCC-BY-NC 4.0 International license.

1479 Yang, Y., Torchinsky, M.B., Gobert, M., Xiong, H., Xu, M., Linehan, J.L., Alonzo, F., Ng, C., Chen,
1480 A., Lin, X*., et al.* (2014). Focused specificity of intestinal TH17 cells towards commensal
1481 bacterial antigens. Nature *510*, 152-156.
1482 Yuan, J., Bennett, B.D., and Rabinowitz, J.D. (2008). Kinetic flux profiling for quantitation of
1483 cellular metabolic fluxes. Nat Protoc *3*, 1328-1340.
1484 Zaidi, A.U., Kedar, P., Koduri, P.R., Goyette, G.W., Buck, S., Paglia, D.E., and Ravindranath, Y.
1485 (2017). Glucose phosphate isomerase (GPI) Tadikonda: Characterization of a novel
1486 Pro340Ser mutation. Pediatr Hemat Oncol *34*, 449-454.
1487 Zanella, A., Fermo, E., Bianchi, P., and Valentini, G. (2005). Red cell pyruvate kinase deficiency:
1488 molecular and clinical aspects. Br J Haematol *130*, 11-25.
1489 Zhao, D., Badur, M.G., Luebeck, J., Magana, J.H., Birmingham, A., Sasik, R., Ahn, C.S., Ideker, T.,
1490 Metallo, C.M., and Mali, P. (2018). Combinatorial CRISPR-Cas9 Metabolic Screens Reveal
1491 Critical Redox Control Points Dependent on the KEAP1-NRF2 Regulatory Axis. Mol Cell *69*,
1492 699-708 e697.
1493 Zheng, Y., Danilenko, D.M., Valdez, P., Kasman, I., Eastham-Anderson, J., Wu, J., and Ouyang, W.
1494 (2007). Interleukin-22, a T(H)17 cytokine, mediates IL-23-induced dermal inflammation and
1495 acanthosis. Nature *445*, 648-651.
1496
1497
1498
1499
1500
1501

bioRxiv preprint doi: https://doi.org/10.1101/857961; this version posted November 29, 2019. The copyright holder for this preprint (which was not certified by peer review) is the author/funder, who has granted bioRxiv a license to display the preprint in perpetuity. It is made available under aCC-BY-NC 4.0 International license.

1502

1503

1504

1505

bioRxiv preprint doi: https://doi.org/10.1101/857961; this version posted November 29, 2019. The copyright holder for this preprint (which was not certified by peer review) is the author/funder, who has granted bioRxiv a license to display the preprint in perpetuity. It is made available under aCC-BY-NC 4.0 International license.

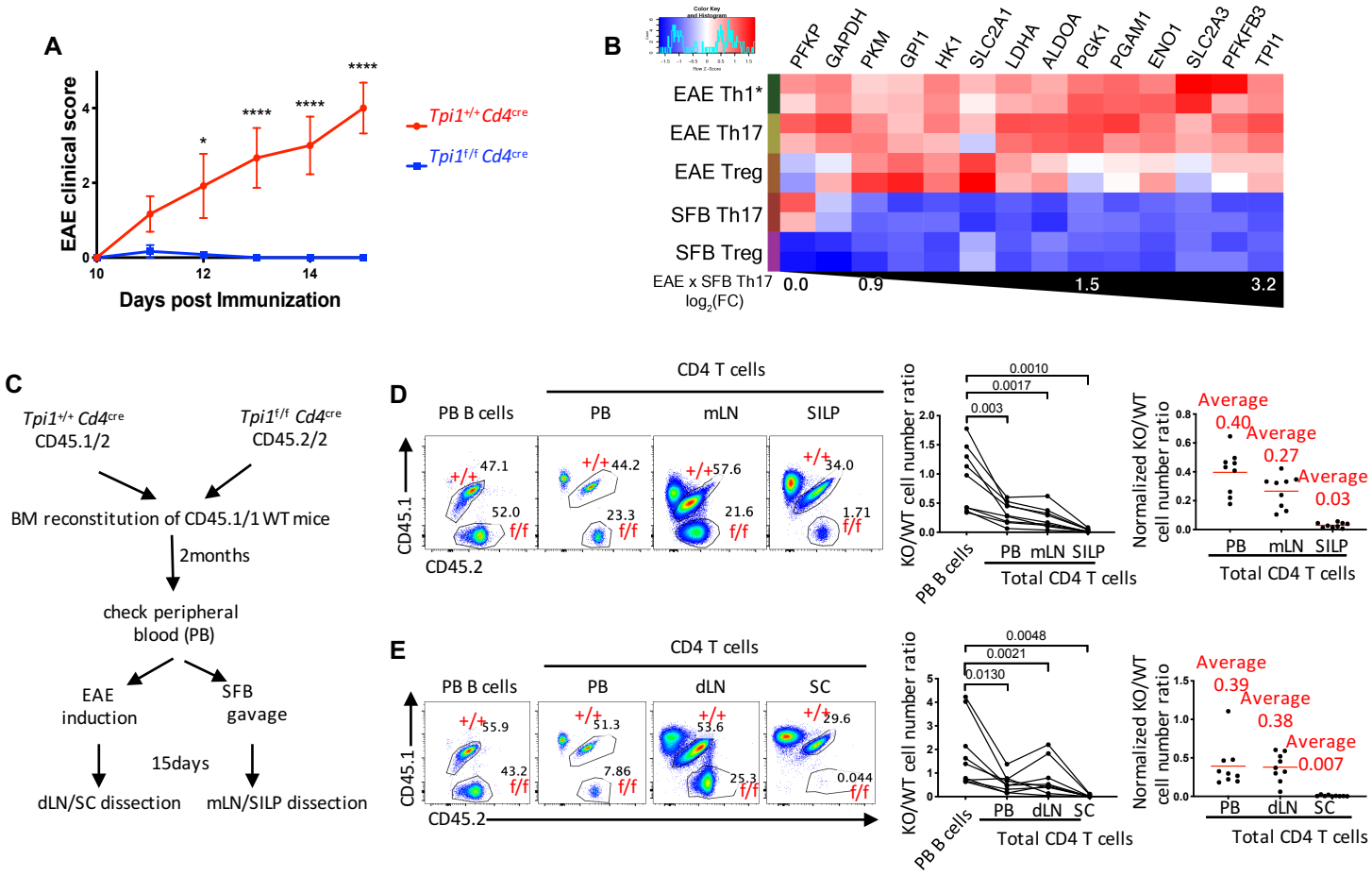

bioRxiv preprint doi: https://doi.org/10.1101/857961; this version posted November 29, 2019. The copyright holder for this preprint (which was not certified by peer review) is the author/funder, who has granted bioRxiv a license to display the preprint in perpetuity. It is made available under aCC-BY-NC 4.0 International license.

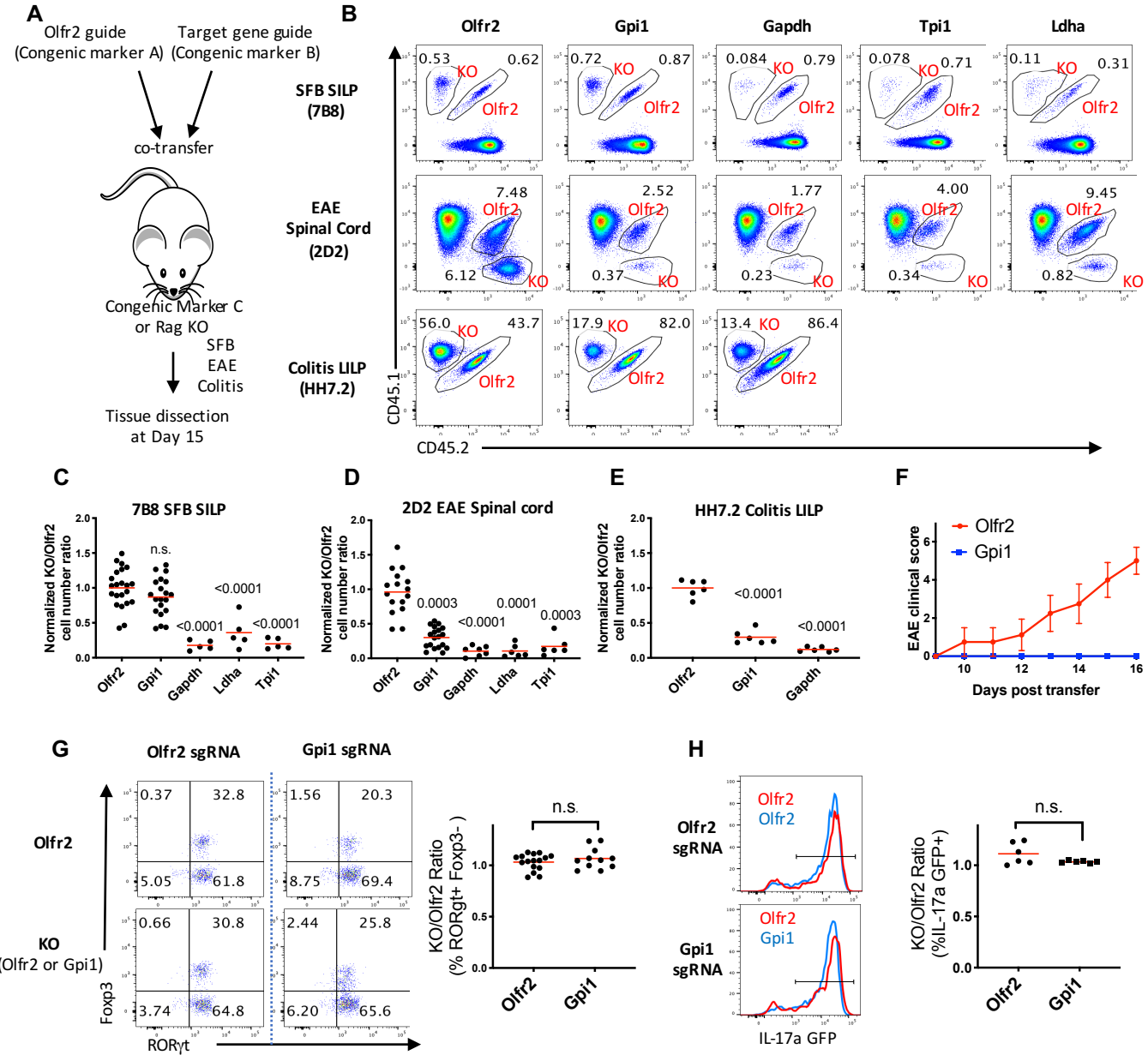

bioRxiv preprint doi: https://doi.org/10.1101/857961; this version posted November 29, 2019. The copyright holder for this preprint (which was not certified by peer review) is the author/funder, who has granted bioRxiv a license to display the preprint in perpetuity. It is made available under aCC-BY-NC 4.0 International license.

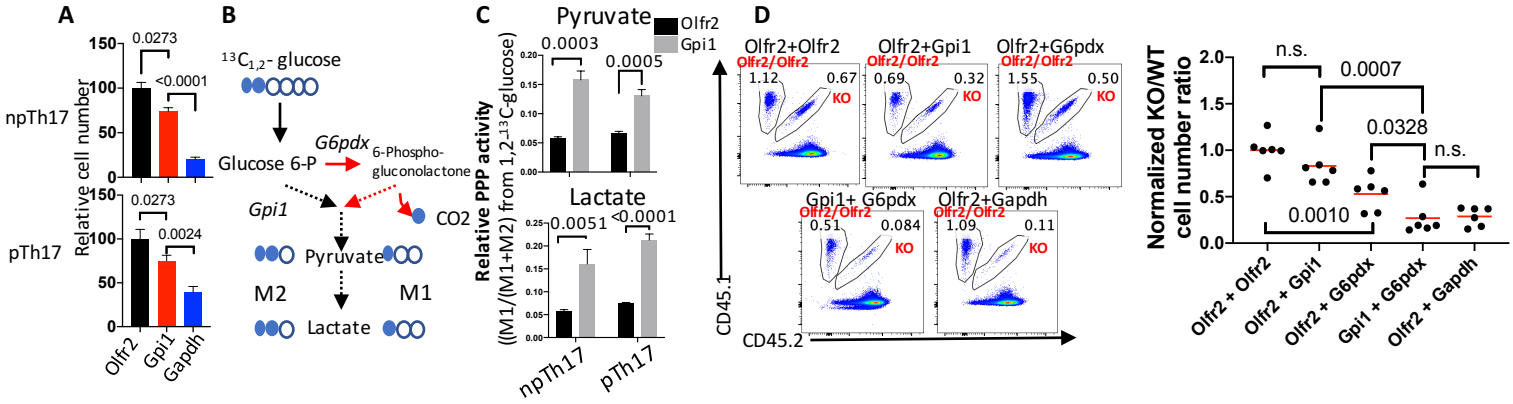

bioRxiv preprint doi: https://doi.org/10.1101/857961; this version posted November 29, 2019. The copyright holder for this preprint (which was not certified by peer review) is the author/funder, who has granted bioRxiv a license to display the preprint in perpetuity. It is made available under aCC-BY-NC 4.0 International license.

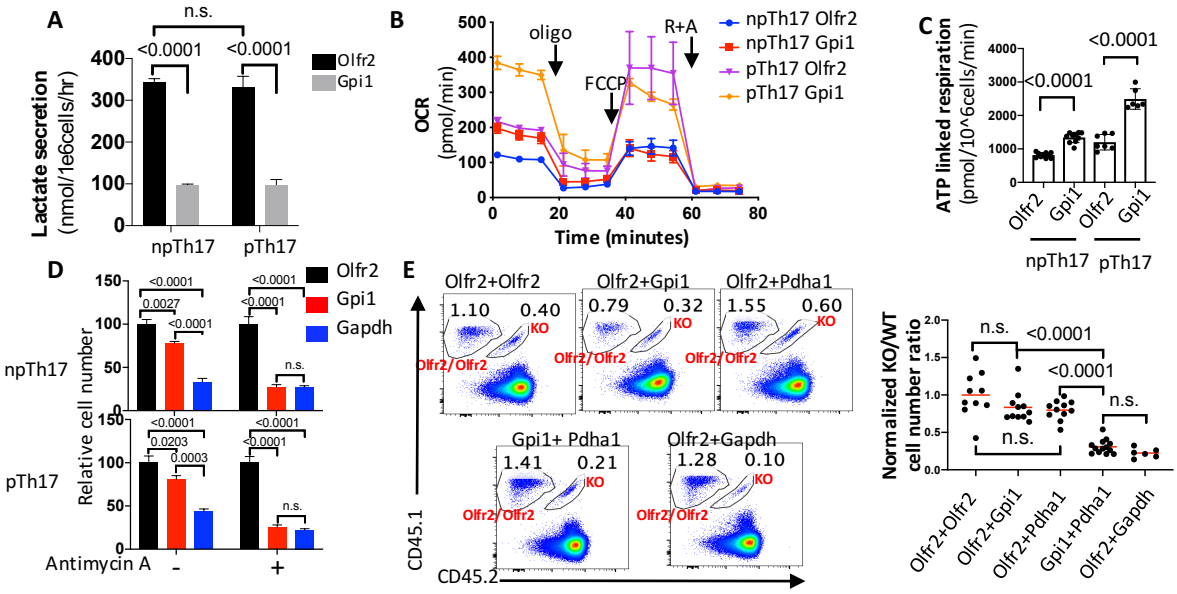

bioRxiv preprint doi: https://doi.org/10.1101/857961; this version posted November 29, 2019. The copyright holder for this preprint (which was not certified by peer review) is the author/funder, who has granted bioRxiv a license to display the preprint in perpetuity. It is made available under aCC-BY-NC 4.0 International license.

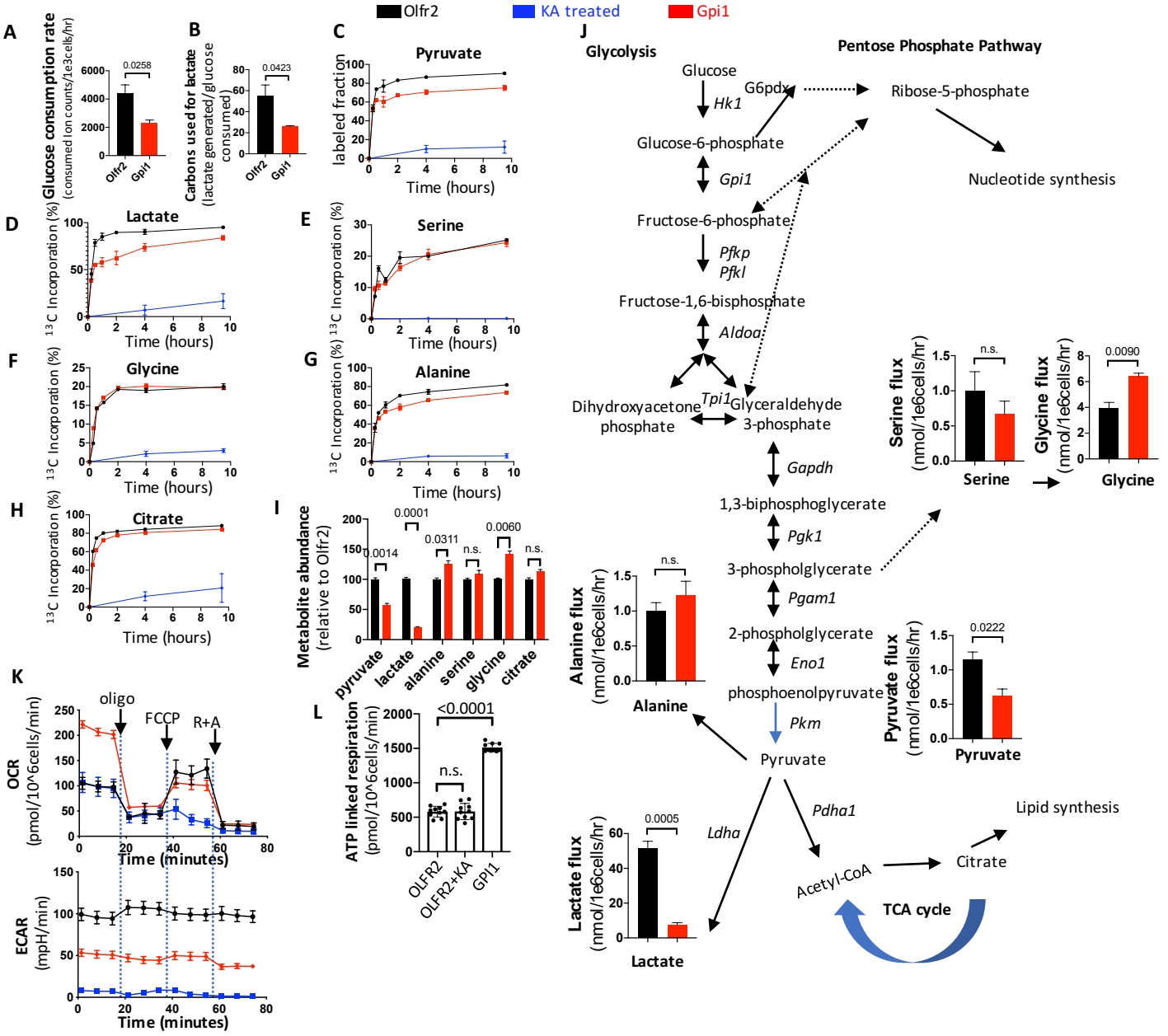

bioRxiv preprint doi: https://doi.org/10.1101/857961; this version posted November 29, 2019. The copyright holder for this preprint (which was not certified by peer review) is the author/funder, who has granted bioRxiv a license to display the preprint in perpetuity. It is made available under aCC-BY-NC 4.0 International license.

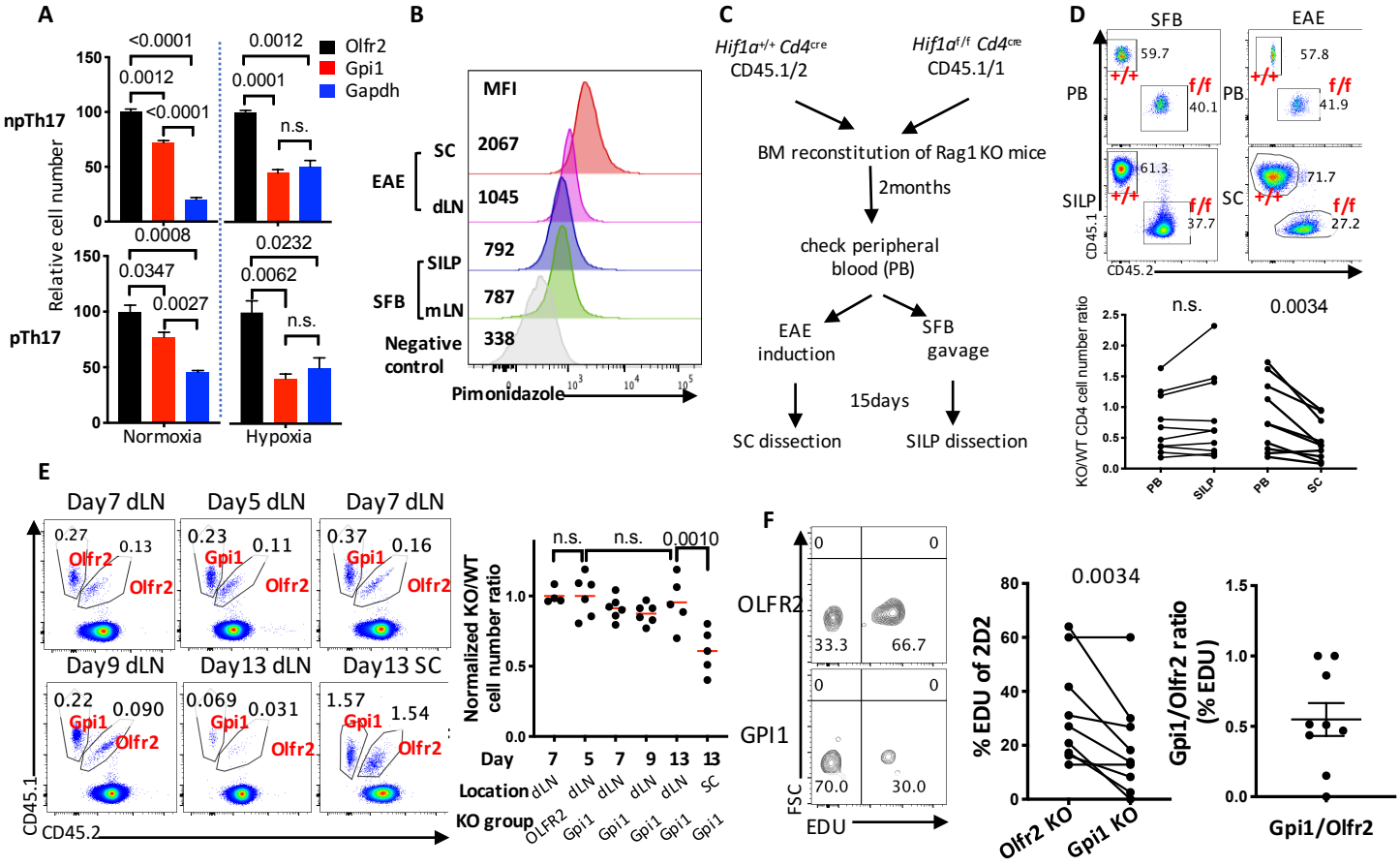

bioRxiv preprint doi: https://doi.org/10.1101/857961; this version posted November 29, 2019. The copyright holder for this preprint (which was not certified by peer review) is the author/funder, who has granted bioRxiv a license to display the preprint in perpetuity. It is made available under aCC-BY-NC 4.0 International license.

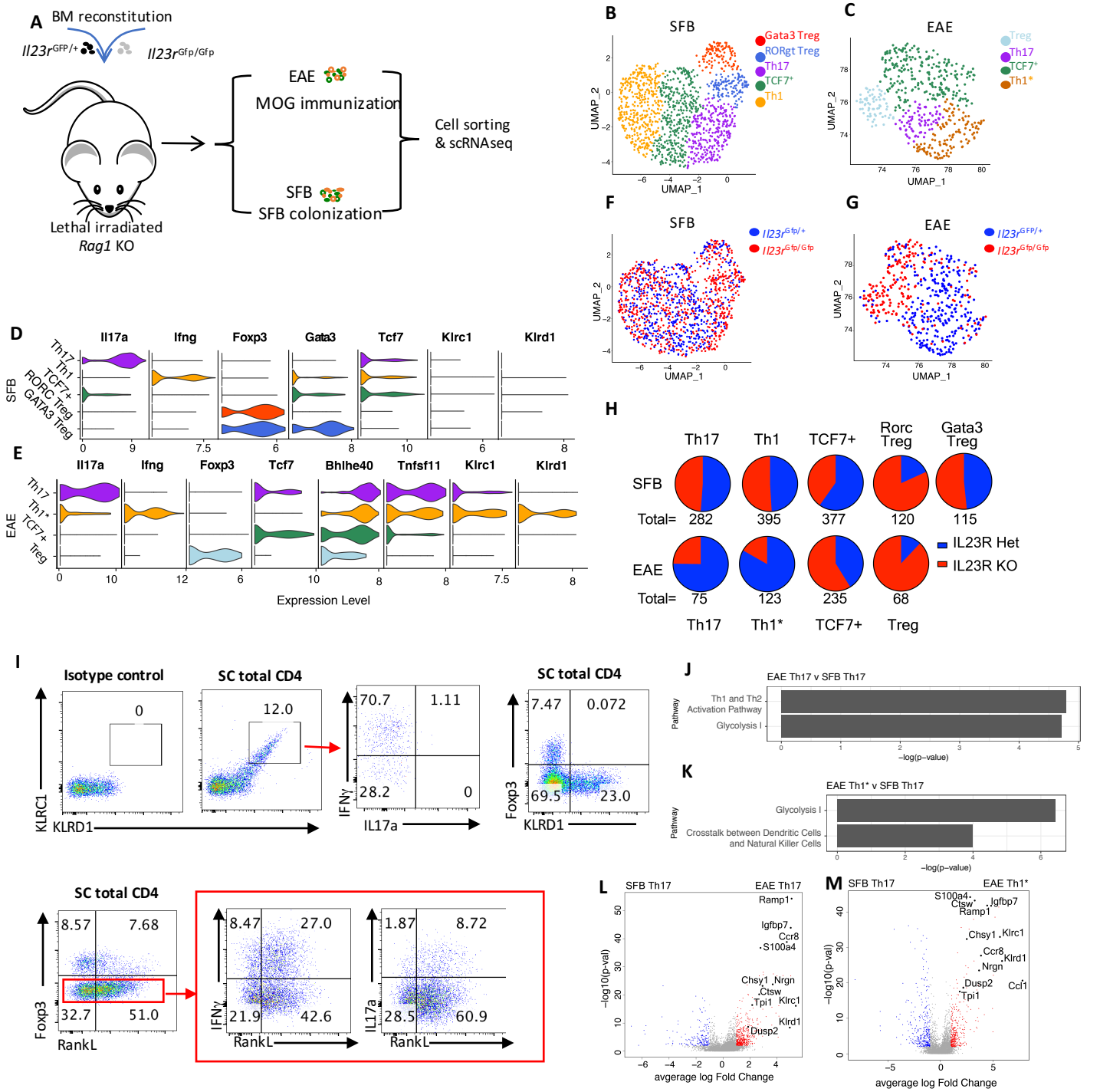

bioRxiv preprint doi: https://doi.org/10.1101/857961; this version posted November 29, 2019. The copyright holder for this preprint (which was not certified by peer review) is the author/funder, who has granted bioRxiv a license to display the preprint in perpetuity. It is made available under aCC-BY-NC 4.0 International license.

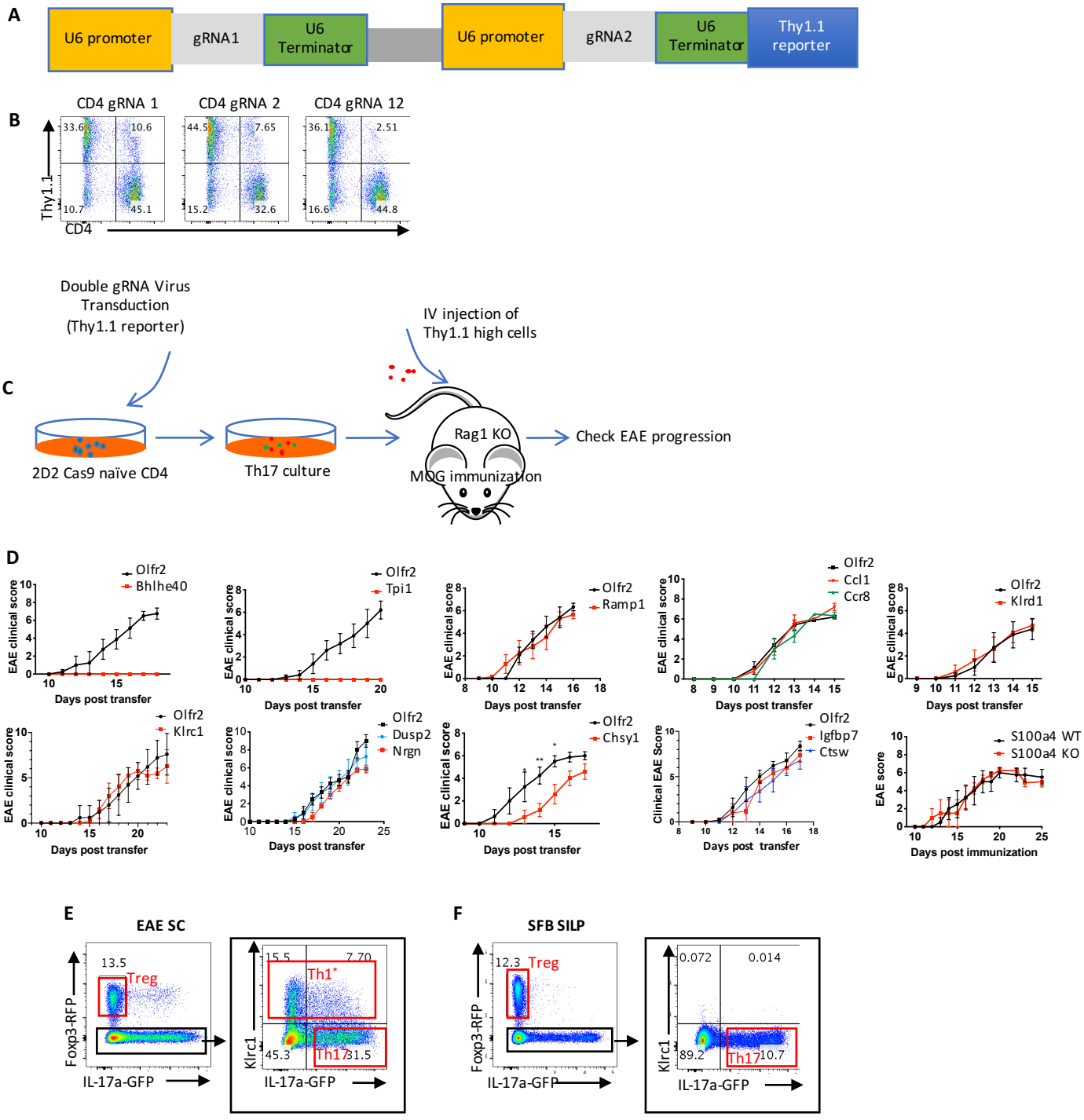

bioRxiv preprint doi: https://doi.org/10.1101/857961; this version posted November 29, 2019. The copyright holder for this preprint (which was not certified by peer review) is the author/funder, who has granted bioRxiv a license to display the preprint in perpetuity. It is made available under aCC-BY-NC 4.0 International license.

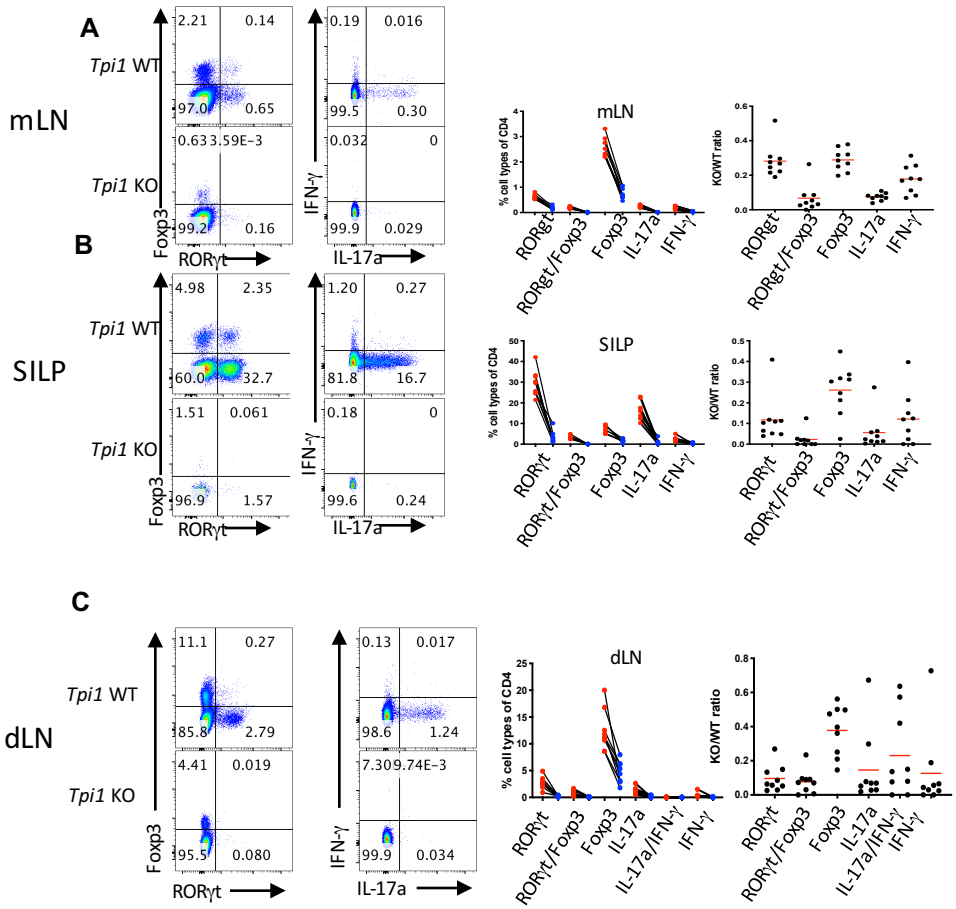

bioRxiv preprint doi: https://doi.org/10.1101/857961; this version posted November 29, 2019. The copyright holder for this preprint (which was not certified by peer review) is the author/funder, who has granted bioRxiv a license to display the preprint in perpetuity. It is made available under aCC-BY-NC 4.0 International license.

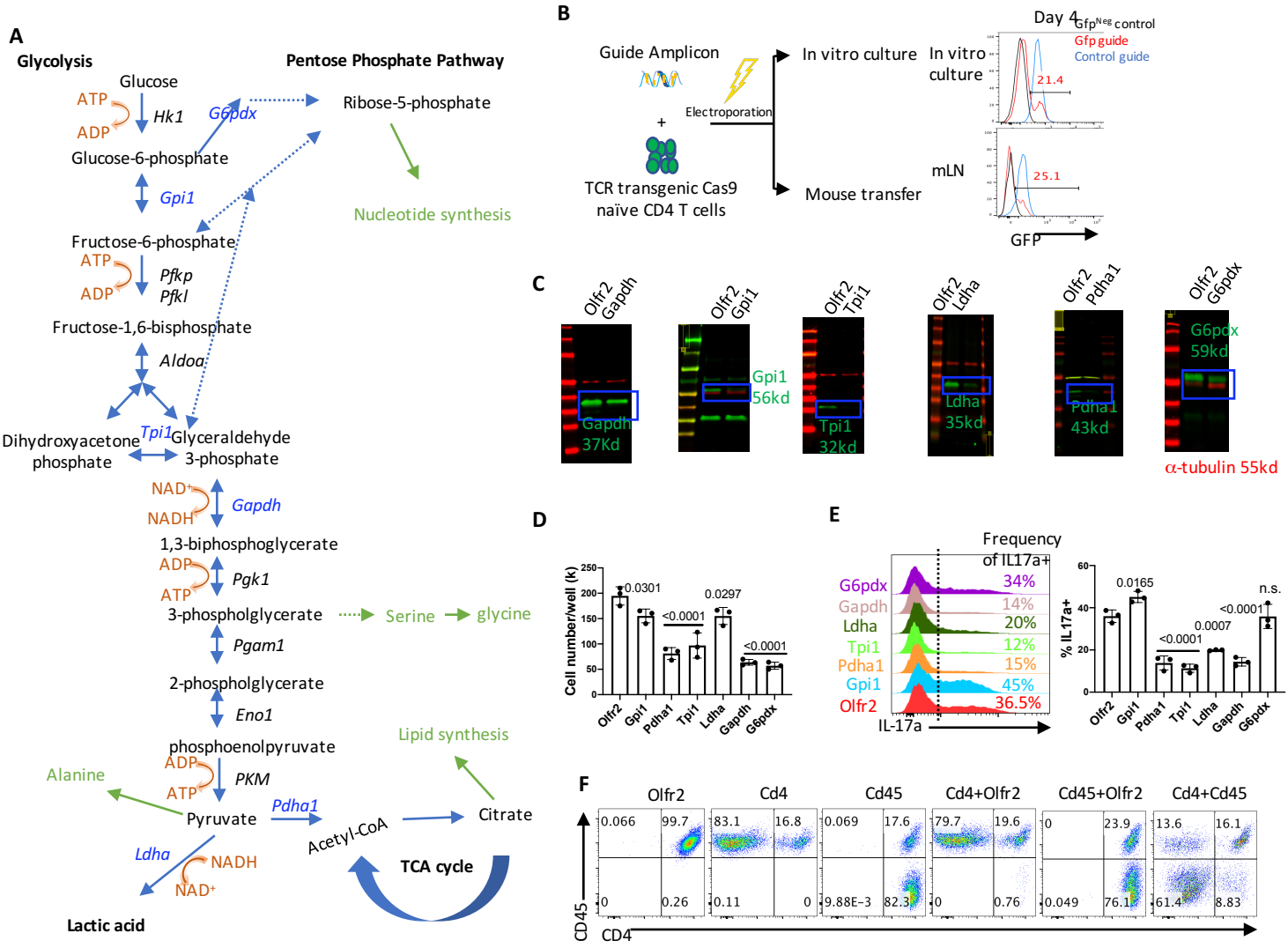

bioRxiv preprint doi: https://doi.org/10.1101/857961; this version posted November 29, 2019. The copyright holder for this preprint (which was not certified by peer review) is the author/funder, who has granted bioRxiv a license to display the preprint in perpetuity. It is made available under aCC-BY-NC 4.0 International license.

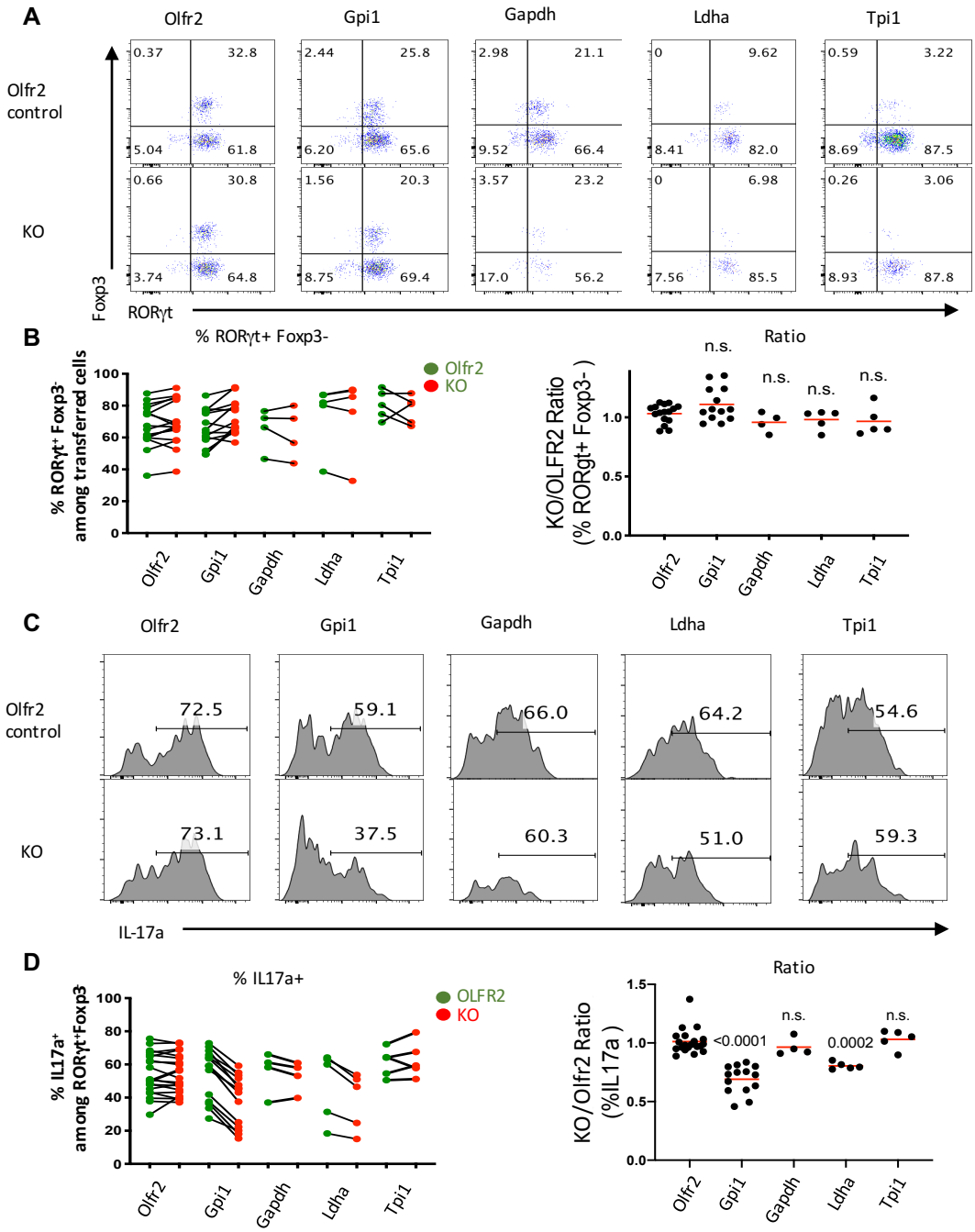
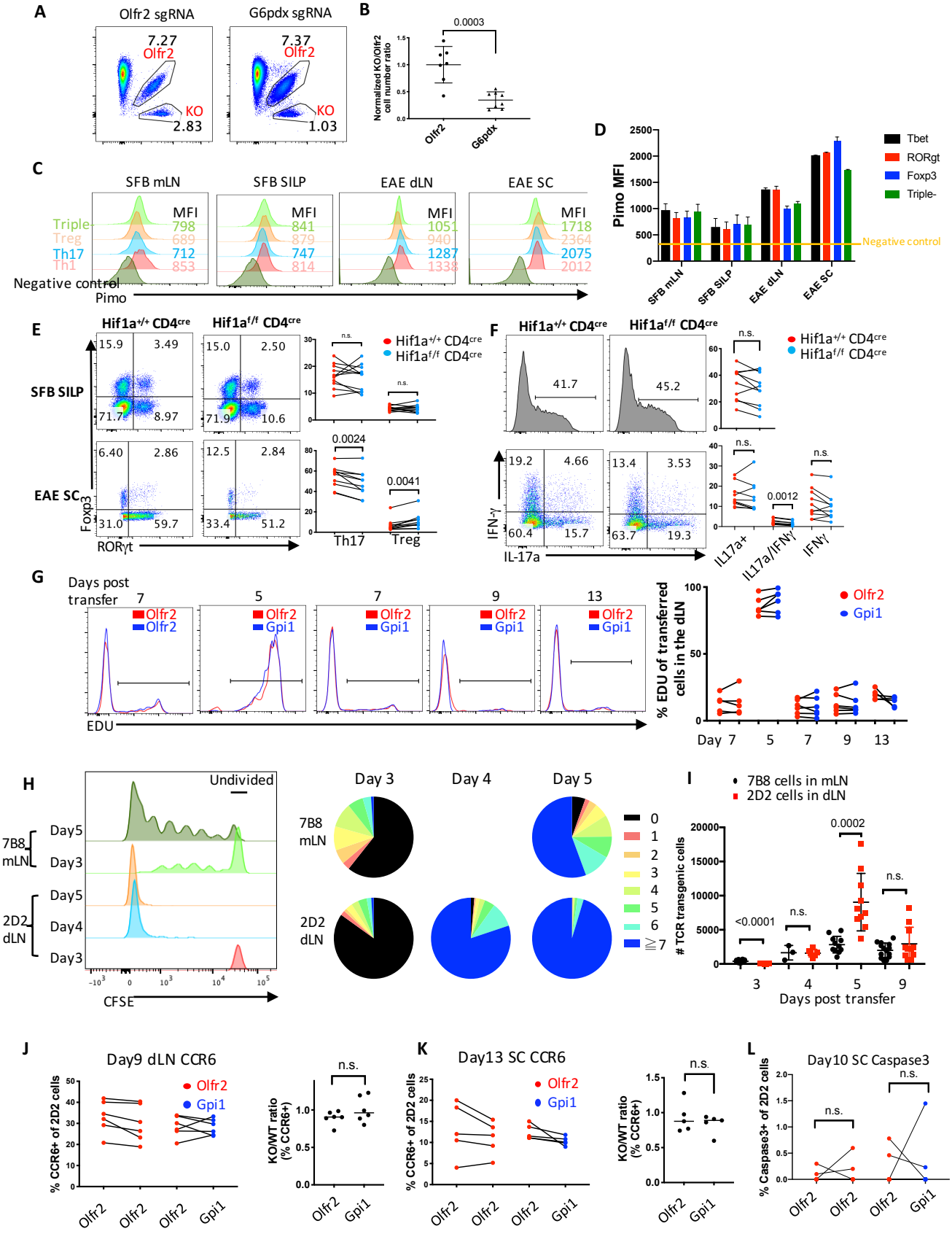
bioRxiv preprint doi: https://doi.org/10.1101/857961; this version posted November 29, 2019. The copyright holder for this preprint (which was not certified by peer review) is the author/funder, who has granted bioRxiv a license to display the preprint in perpetuity. It is made available under aCC-BY-NC 4.0 International license.